The Journal of
Undergraduate Research
in Physics

CONTENTS

Volume 17, Number 2
Spring 1999

Produced by the Physics Department of Guilford College
for
The American Institute of Physics and the Society of Physics Students

Please
wh

TH[illegible]URNAL OF UNDERGRADUATE RESEARCH IN PHYSICS

Th[illegible]ournal is devoted to research work done by undergraduate students in physics and its related fields. It is a vehicle for the exchange of ideas and information by undergraduate students. Information for students wishing to submit manuscripts for possible inclusion in the Journal follows.

ELIGIBILITY
The author(s) must have performed all work reported in the paper as an undergraduate student(s). The subject matter of the paper is open to any area of pure or applied physics or physics related field.

SPONSORSHIP
Each paper must be sponsored by a full-time faculty member of the department in which the research was done. A letter from the sponsor, certifying that the work was done by the author as an undergraduate and that the sponsor is willing to be acknowledged at the end of the paper, must accompany the manuscript if it is to be considered for publication.

SUBMISSION
Two copies of the manuscript, the letter from the sponsor and a telephone number or E-Mail address where the author can be reached should be sent to:
Dr. Rexford E. Adelberger, Editor
THE JOURNAL OF UNDERGRADUATE RESEARCH IN PHYSICS
Physics Department
Guilford College
Greensboro, NC 27410

FORM
The manuscript should be typed, double spaced, on 8 1/2 x 11 inch sheets. Margins of about 1.5 inches should be left on the top, sides, and bottom of each page. Papers should be limited to fifteen pages of text in addition to an abstract (not to exceed 250 words) and appropriate drawings, pictures, and tables. Manuscripts may be submitted on a disk that can be read by a MacIntosh™. The files must be compatible with MacWrite™, MicroSoft Word™ , PageMaker™ or WordPerfect™.

ILLUSTRATIONS
Line drawings should be made with black ink on plain white paper. The line thickness should be sufficient to be reduced to column format. Each figure or table must be on a separate sheet. Photographs must have a high gloss finish. If the submission is on a disk, the illustrations should be in PICT, TIFF or EPS format.

CAPTIONS
A descriptive caption should be provided for each illustration or table, but it should not be part of the figure. The captions should be listed together at the end of the manuscript

EQUATIONS
Equations should appear on separate lines, and may be written in black ink. All equations should be numbered. We use EXPRESSIONIST™ to format equations in the Journal.

FOOTNOTES
Footnotes should be typed, double spaced and grouped together in sequence at the end of the manuscript.

PREPARING A MANUSCRIPT
A more detailed set of instructions and advice for authors wishing to prepare manuscripts for publication in the Journal of Undergraduate Research in Physics can be found in the back of each issue.

SUBSCRIPTION INFORMATION

The Journal is published twice each academic year, issue # 1 appearing in the fall and issue # 2 in the spring of the next calendar year. There are two issues per volume.

TYPE OF SUBSCRIBER	PRICE PER VOLUME
Individual	$US 5.00
Institution	$US 10.00

Foreign subscribers add $US 2.00 for surface postage, $US 10.00 for air freight.

Back issues may be purchased by sending $US 15.00 per volume to the editorial office.

To receive a subscription, send your name, address, and check made out to **The Journal of Undergraduate Research in Physics (JURP)** to the editorial office:

JURP
Physics Department
Guilford College
Greensboro, NC 27410

The Journal of Undergraduate Research in Physics is sent to each member of the Society of Physics Students as part of their annual dues.

APPROXIMATING THE OPTIMUM DRIVING PATH THROUGH A CURVE

Mihail Milkov
Department of Physics
Angelo State University
San Angelo, TX 76909
received December 5, 1997

ABSTRACT

The optimum driving path for a vehicle passing through a curve is the one that can be traveled in the least amount of time without skidding the tires. We modeled the path, $y(x)$, as an n^{th} order polynomial. We numerically calculate the time to complete identical length trips through a curve for path functions $y(x) = k_2x^2$, $y(x) = k_2x^2 + k_4x^4$ and $y(x) = k_2x^2 + k_{2n}x^{2n}$. The path $y(x) = k_2x^2 + k_4x^4$ provided both the minimum travel time and the most realistic motion.

INTRODUCTION

Consider a vehicle making a change in its direction of motion of an angle 2α. The optimum driving path is the curved path that the vehicle can take that can be traveled in the least time without skidding the tires. A simple beginning approach to finding the optimum driving path is to consider a path taken along a circle of radius R. [1] The minimum time to make this turn without slipping is:

$$t_{MIN} = 2\,\alpha\sqrt{\frac{R}{\mu\, g}}\,, \qquad (1)$$

where μ is the static coefficient of friction. This driving path causes an abrupt transition in the acceleration perpendicular to the direction of motion when the vehicle makes the transition between straight line motion before entering the curve and the circular motion in the curve. This is not a realistic model for the actual motion of a vehicle. An more realistic model for the optimum driving path (the one that gives the shortest trip) is achieved by having the vehicle travel along a curve that is modeled by a polynomial function.

THE MODEL

A vehicle's motion in a horizontal curve is determined by the driving forces, $F_1 \ldots F_4$ applied at the points of contact of the tires with the road. (See Figure 1). Each of these forces lie in the plane of the road, and points in the direction of the wheels. We choose the forces to be positive when the car is accelerating and negative when the car is decelerating. In the vertical direction, the force due to gravity ($G = mg$) applied at the center of mass of the car, S, is balanced by the vertical reactions, $G_1 \ldots G_4$, of the road.

In this paper, we consider a non-inertial reference frame, the reference frame of the moving car. This is a common approach for reducing a dynamic problem to a static problem. In this reference frame, the forces that oppose any changes in the motion of the vehicle are called

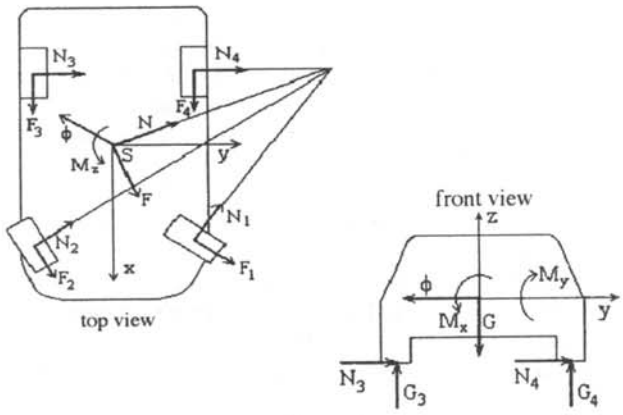

Figure 1
Schematic diagram of the car traveling along the path through a curve, showing the forces acting on the wheels and the moments.

Mihail Milkov completed this individual research project in his junior year as a physics/computer science major at Angelo State University. The incentive for this topic came from Mihail's own keen interest in car racing. Mihail graduated summa cum laude in 1998 and is now a graduate student in electrical engineering at UCLA. In his spare time, Mihail enjoys skiing, hiking and reading.

'inertial forces'. Since we are considering an object (not just a point mass), these forces act at different points of the object. The net inertial force and the net inertial moment are equal in magnitude but opposite in direction to the net force and net moment acting on the vehicle. In the frame of reference of the car, the inertial forces acting on the car, summed at the center of mass, reduce to a force, $\vec{\phi}$, and moment, $\vec{M}_\phi$,:

$$\vec{\phi} = -m\,\vec{a} \qquad (2)$$
$$\vec{M}_\phi = -I_\phi\,\vec{\varepsilon}\,,$$

where m is the mass, I_z is the moment of inertia of the car, a the acceleration of the center of mass and ε the angular acceleration. The force and moment in Equation 2 are opposed by the lateral reactions N_1 ... N_4 applied at the point of contact of the tires. (See Figure 1).

When the driving forces and the lateral reactions are summed at the center of mass, moments M_x and M_y appear. The moment M_x causes the load to redistribute between the inside and the outside (relative to the curve) wheels, while the moment M_y causes a load redistribution between the front and rear axles. These redistributions will not lead to skidding if the car is equipped with an active system for optimum distribution of the driving forces among the four wheels. The effect of the moment M_z can be ignored when the angular acceleration varies smoothly

Thus, the inertial force, $\vec{\phi}$, is balanced by the resultant driving force, $\vec{F}$, and the resultant lateral force, $\vec{N}$. If there is to be no skidding, the vector sum of these two forces must satisfy the condition:

$$\left|\vec{F} + \vec{N}\right| \le \mu\, m\, g\ , \qquad (3)$$

where μ is the static coefficient of friction between the tires and the road. Since forces $\vec{F}$ and $\vec{N}$ are perpendicular to each other, we may write Equation 3 as:

$$\sqrt{a_n^2 + a_t^2} = \mu\, g\,, \qquad (4)$$

where a_n is the acceleration perpendicular to the direction of motion and a_t is the acceleration tangent to the direction of motion. The inequality has been replaced by an equality because the curve with the smallest time will be the case just before skidding starts.

In our analysis, we make the following restrictions and simplifications:

- The aerodynamic down force is excluded.
- The engine has enough power to produce maximum tangential acceleration at any speed.
- The car is equipped with active driving force redistribution system.
- The line on which the vector $\vec{a_n} + \vec{a_t} + \vec{g}$ lies crosses the surface of the road within the four contact points of the tires. This means that the car cannot overturn.
- The speed on entering and exiting the curve is the same and the acceleration has to change smoothly.
- The driving path for the curve is symmetric relative to the bisector of the curve.
- The driving path is a continuous function so that the velocity has smooth changes in direction.
- The derivative of the driving path curve must be a continuous function so that the acceleration can vary smoothly.

To find the optimum driving path, we vary the geometric parameters and determine the kinematic parameters from Equation 4.

SETUP FOR THE PROBLEM

Figure 2 shows a schematic road curve of angle 2α and full width $w + 2r$ where $2r$ is the width of the car and w, the effective width, is the region where the center of mass of the car can be. The distance CO in Figure 2 is determined geometrically as:

$$CO = \frac{w + r}{\cos(\alpha)} - r\,. \qquad (5)$$

Each driving path will contain two equal straight portions, $AM = NB$ and a curved portion, MON. To compare the times for taking the curve along different driving paths, we must have the vehicle travel a constant distance $d = AC = BC$ from the corner C of the curve for each of the different paths. The curved portions of the various paths begin and end at different distances $c = CM = CN$ from the corner of the curve. In our model, the distance d will always be greater the than greatest c we have for all driving paths. The cars will move from point A to point M to point N to point B. We shall compare the total driving time, t_{total} for different driving paths:

$$t_{total} = t_{MN} + 2\,t_{AM}\ , \qquad (6)$$

where t_{MN} is the time to travel along the curved part of the path and t_{AM} is the time to travel along the straight part of the path.

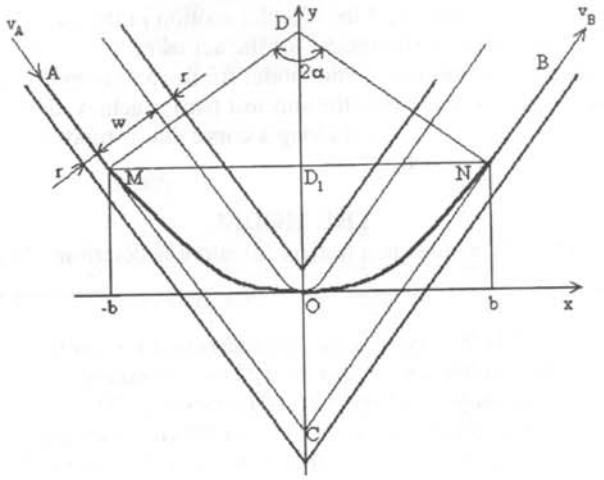

Figure 2
Schematic diagram of the road curve and a driving path showing the semichord distance b and the curve angle 2α.

All of the various paths taken must be tangent to the x axis at $x = 0$. At this point, there will only be an x component to the velocity. Since the y component of the velocity is negative for $x < 0$ and positive for $x > 0$, the smallest value for the speed, v_{min} occurs when $x = 0$:

$$v(x=0) = v_x(x=0) = v_{\min} . \quad (7)$$

Equation 7 implies that the tangential acceleration, a_t, changes sign at $x = 0$. Since the acceleration is continuous, $a_t(x=0) = 0$. Using this result in Equation 4 we find that for any driving curve the maximum acceleration, a_{max} is:

$$a(x=0) = a_n(x=0) = a_{\max} = \mu g . \quad (8)$$

POLYNOMIAL DRIVING PATHS

The optimum driving path is modeled as an even polynomial function, $y(x)$, passing through the origin:

$$y(x) = k_2 x^2 + k_4 x^4 + \ldots + k_{2n} x^{2n} + \ldots , \quad (9)$$

where the coefficients, k_2, k_4, ... are determined by a number of constraints. First, the curve has to be tangent to the curb lines CA and CB (see Figure 2):

$$\frac{dy}{dx}(b) = 2k_2 b + 4k_4 b^3 + \ldots + 2n\, k_{2n}\, b^{2n-1} + \ldots = \tan(\alpha). \quad (10)$$

Second, the points M and N must be inflection points:

$$\frac{d^2y}{dx^2}(b) = 2k_2 + 12k_4 b^2 + \ldots + 2n(2n-1)k_{2n} b^{2n-2} + \ldots = 0. \quad (11)$$

The third restriction will be for scaling the function to the size of the curve. Examination of the triangle CMD in Figure 2 gives:

$$y(b) = b \tan(\alpha) - CO \quad (12)$$

where:

$$b = M D_1 = D_1 N \quad (13)$$

is the semichord of the curve. Substituting Equation 5 into Equation 12 gives:

$$y(b) = r + b \tan(\alpha) - \frac{w + r}{\cos(\alpha)} . \quad (14)$$

The radius of curvature, ρ, of the curve can be found using the well-known formula:

$$\rho(x) = \frac{1}{y''(x)}\left[1 + \left(y'(x)\right)^2\right]^{\frac{3}{2}} . \quad (15)$$

Evaluating Equations 9 and 15 at $x = 0$ gives:

$$\rho(0) = \frac{1}{2 k_2} . \quad (16)$$

The radius of curvature must be finite everywhere inside the curve MN, so Equation 16 implies that $k_2 > 0$.

Using Equations 10, 11, and 14, the semichord b and two of the coefficients k_2, k_4, k_6, ... can be found. The remaining coefficients must be varied to find the driving path with the least t_{total}. Notice that the speed v_o for entering and exiting the driving path AOB and the speed v_1 for entering and exiting the curved portion MN of the driving path are different for different k coefficients.

Parabolic Driving Path

The simplest polynomial path is a parabolic one, where the only k coefficient that is not zero is k_2. Using Equation 10 to evaluate k_2, we obtain:

$$y(x) = k_2 x^2 = \frac{\tan(\alpha)}{2b} x^2 . \quad (17)$$

Using Equations 14 and 17, we find the semichord:

$$b = \frac{2}{\sin(\alpha)}\left[w + r(1 - \cos(\alpha))\right] . \quad (18)$$

From Equation 16, the radius of curvature of the path at $x = 0$ is:

$$\rho(0) = \frac{1}{2 k_2} = b \cot(\alpha) . \quad (19)$$

Since the y component of the velocity is zero at $x = 0$ and the centripetal acceleration is supplied by friction:

$$v_x(x=0) = v(x=0) = \sqrt{\mu g \rho(0)} = \sqrt{\mu g b \cot(\alpha)} . \quad (20)$$

For parabolic motion, the x component of the velocity is constant. The time for moving along the parabolic path is determined by v_x and the semichord length b:

$$t_{MN} = \frac{2b}{v_x} = 2\sqrt{\frac{b \tan(\alpha)}{\mu g}} . \quad (21)$$

Notice that for the parabolic driving path:

$$\frac{d^2y}{dx^2}(x) = \frac{\tan(\alpha)}{b} = \text{constant} \neq 0 \quad (22)$$

which contradicts constraint given by Equation 11. This is because the radius of curvature at the points M and N is not infinity, so the acceleration is not continuous at these points.

The speed, v_1, for entering and exiting the curved path can be determined from v_x by noticing that v_1 makes an angle α with v_x at the point M:

$$v_1 = \frac{v_x}{\cos(\alpha)} = \sqrt{\frac{2\mu g b}{\sin(2\alpha)}} . \quad (23)$$

At any point on the parabola, the total acceleration $a = \mu g$ = constant and is in the direction of the y axis. If α_M is the instantaneous angle between a and a_n, then $\tan(\alpha_M) = y'(x)$ and

$$a_n = a\cos(\alpha_M) = \frac{a}{\sqrt{1 + \tan^2(\alpha_M)}} = \frac{\mu g}{\sqrt{1 + \left(y'(x)\right)^2}} = \frac{\mu g}{\sqrt{1 + \left(\frac{\tan(\alpha)}{b}\right)^2 x^2}} . \quad (24)$$

Again there is a jump in a_n when we enter the curve, but Equation 24 shows that this value is always less than μg, the value for the circular path.

The Quartic Driving Path

In this path, we use the first two terms of Equation 9. This path curve will satisfy Equation 11 for smooth acceleration change. The coefficients k_2 and k_4 can be found using Equations 10 and 11:

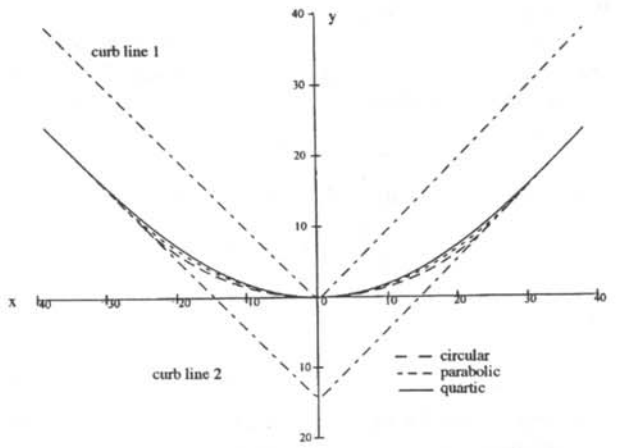

Figure 3
Diagram of the three driving paths showing the curb lines for a 90° bend.

$$y(x) = k_2x^2 + k_4x^4 = \frac{3}{4}\frac{\tan(\alpha)}{b}x^2 - \frac{1}{8}\frac{\tan(\alpha)}{b^3}x^4 . \quad (25)$$

From Equation 14, the semichord is:

$$b = \frac{8}{3}\frac{w + r(1-\cos(\alpha))}{\sin(\alpha)} . \quad (26)$$

The curvature of the path at $x = 0$ comes from Equation 16:

$$\rho(0) = \frac{2}{3} b \cot(\alpha) . \quad (27)$$

Using Equation 7 the x component of the velocity at $x = 0$ becomes:

$$v_x(x=0) = \sqrt{\rho(0)\,\mu\, g} = \sqrt{\frac{2}{3} b \cot(\alpha)\,\mu\, g} . \quad (28)$$

In contrast to the parabolic path, v_x is not constant. It increases with the increase in x. Because v_x is not constant, the calculation of the time t_{MN} is much more difficult. A numerical solution for the particular initial conditions has to be used. The known values for the acceleration (Equation 8) and the velocity (Equation 28) and the starting position $x = 0$ are the initial conditions in an iterative calculation:

1 Find y' (Equation 10), y'' (Equation 11) and ρ (Equation 15).
2 Find a_n from ρ and v, and a_t from Equation 4.
3 Find:

$$v(t + dt) = v(t) + a_t\, dt , \quad (29)$$

and use

$$v_x = v\cos(\alpha_M) = \frac{v}{\sqrt{1+\tan^2(\alpha_M)}} = \frac{v}{\sqrt{1+\left(y'(x)\right)^2}} \quad (30)$$

to get $v_x(t+dt)$.
4 Find:

$$x(t + dt) = x(t) + v_x(t + dt)\, dt . \quad (31)$$

5 Increment t by dt and repeat until $x = b$ (from Equation 26).

The final value of t will be t_{MN} and the final value of v will be v_1.

Polynomial Driving Paths of Higher Powers

Now we consider the path curve function

$$y(x) = k_2x^2 + k_{2n}x^{2n} . \quad (32)$$

It has two unknown coefficients which are obtained in the same manner as Equation 25:

$$k_2 = \frac{1}{4}\frac{2n-1}{n-1}\frac{\tan(\alpha)}{b}$$
$$k_{2n} = -\frac{1}{4}\frac{1}{n(n-1)}\frac{\tan(\alpha)}{b^{2n-1}} , n \geq 2 \quad (33)$$

We obtain the semichord b from Equation 14 and then, as we did for Equations 27 and 28, we obtain $\rho(0)$ and $v_x(0)$. Once again, the numerical method is used to find t_{MN}.

From Equation 33, as n is increased:

$$k_2 \to \frac{\tan(\alpha)}{2b} , \; k_{2n} \to 0 , \quad (34)$$

The curve will look more and more like the parabolic curve as n increases. Consequently, the acceleration jump at the points M and N will become larger, approaching that of the parabolic path.

COMPARISON OF THE VARIOUS PATHS

Finding the total path length

The semichord b is smallest for the circular driving path, larger for the parabolic driving path and largest for the quartic driving path. The distance, c, from the corner to where the curved path begins is given by:

$$c = CM = CN = \frac{b}{\cos(\alpha)} \quad (35)$$

The distance c is important because it sets the minimum value for d, the strip of road along which the total time, t_{total}, is measured. Since c is greatest for the quartic driving path, we will set $d = C_{quartic}$ for the time measurements.

Parameter		Driving Path Circular	Parabolic	Quartic
b	[m]	24.85	29.11	38.82
c	[m]	35.14	41.17	54.90
ρ_{min}	[m]	35.14	29.11	25.88
ρ_{max}	[m]	35.14	82.33	∞
$a_{n\,min}$	[m/s²]	10.00	7.07	0
v_o	[m/s]	27.32	29.27	29.92
v_1	[m/s]	18.74	24.13	29.92
v_{min}	[m/s]	18.74	17.06	16.09
t_{MN}	[s]	2.945	3.412	4.440
t_{total}	[s]	4.661	4.440	4.440

Table 1
Results of calculations for various paths. The curve bends 90°, the effective width of the road is 10 m, μg = 10 m/s² and d = 54.90 m.

The general behavior of the vehicle is to start at speed v_o, decelerate along AM with $a = -\mu g$ to reach speed v_1 at the beginning of the curved section of the path. The time t_{AM} required for this part of the trip is found using the kinematic equation for constant acceleration:

$$v_o = \sqrt{v_1^2 + 2\,\mu\, g\,(d-c)}\,, \tag{36}$$

where c and v_1 depend on the particular driving path. Then:

$$t_{AM} = t_{NB} = \frac{v_o - v_1}{\mu\, g}\,. \tag{37}$$

and from Equation 5 the total driving time is:

$$t_{total} = t_{MN} + 2\,\frac{v_o - v_1}{\mu\, g}\,. \tag{38}$$

Comparative Data

To compare the three driving paths shown in Figure 3, we will assume the following typical road parameters:
w = 10 m (The road is 12 m wide and the car is 2 m wide)
r = 1 m
$\alpha = \pi/4$ (The turn is a 90° bend)
μg = 10 m/s² (1.0 g lateral road holding acceleration)

We use a total driving distance d = 54.9 m.

The results of the calculations are shown in Table 1. Figure 4 shows the speed along the three driving paths. The components of the acceleration, a_n and a_t, along the three driving paths are shown in Figure 5.

Discussion

Examination of the results shown in Table 1 indicate that the parabolic and quartic driving paths are superior to the circular driving path because they require significantly less time. The higher entrance and exit speeds ensure smaller total time although the time in the curved part of the path is larger.

The only real advantage of the circular path is that there is no tangential acceleration during the travel along the curved part of the path. This means that there is no redistribution of weight, so a vehicle without an active driving force distribution system could use this path.

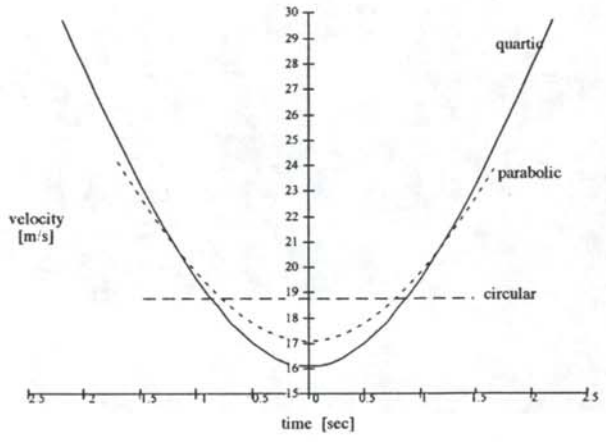

Figure 4
The speed of the vehicle along the three paths.

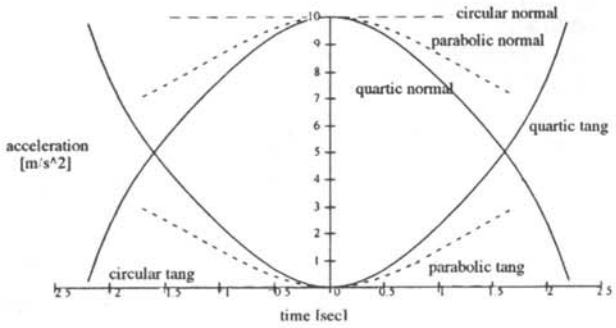

Figure 5
The normal and tangential components of the acceleration for the travel along the three driving paths.

The quartic driving path is nearly identical in shape and time to the parabolic driving path but has the advantage over the circular and parabolic driving paths in that the jump in a_n is not present. The quartic driving path would be the most realistic optimum path to take through a curve.

REFERENCES

* Current address of author: 3721 Mentone Avenue, #4, Los Angeles, CA 90034 MMilkov@ee.ucla.edu

1. J.R. Ellis, Vehicle Handling Dynamics, Mechanical Engineering Publications, London, 1994.; R.M. Brach, "Vehicle Dynamics Model for Simulation on a Microcomputer", International Journal of Vehicle Design, 12, 4, (1991); M.C. Good, Road Curve Geometry and Driver Behavior, Australian Roach Research Board, (1978); S. Motoyama, "Effect of Traction Force Distribution on Vehicle Dynamics", Vehicle System Dynamics, 22, 5-6, (1993).

FACULTY SPONSOR

Dr. Andrew B. Wallace
Department of Physics
Angelo State University
PO Box 10904, ASU Station
San Angelo, TX 76909
awallace@physics.angelo.edu

PHOTOREFRACTIVE DEFOCUSING EFFECT IN STRONTIUM BARIUM NIOBATE

Jeffery N. Blum *
Department of Physics
Northwest Nazarene College
Nampa, ID 83686
received July 27, 1998

ABSTRACT

The photorefractive effect was used in a molybdenum and chromium doped strontium barium niobate:60 crystal to investigate laser defocusing. A helium-neon laser beam was focused on the crystal while an external electric field was applied opposite to the original polling direction of the crystal.. An imaging system, consisting of a focusing lens and a CCD camera was used to monitor the spot size of the laser, both inside and behind the crystal. The degree of defocsing was found to be proportional to the magnitude of the external electric field. The data seem to indicate that the photorefractive effect in this crystal with an external electric field applied produces a defocusing effect similar to that of a variable focal length defocusing lens.

INTRODUCTION

The Photorefractive Effect

The photorefractive effect is a light induced change in the index of refraction, *n*, of a material. Generally, the index of refraction of materials is constant. However, certain types of crystals experience a change in the index of refraction when a voltage is applied across them in conjunction with a single laser beam passing through them. Only crystals which are noncentrosymmetric, lacking inversion symmetry, exhibit this non linear electro-optic effect: a change in the index of refraction due to the presence of an electric field.

The photorefractive effect has been studied widely since it first was reported in 1967 as optical damage. [1] Since then, applications have been found for the effect that include optical data storage, optical limiters, image processing and holography. In 1993, a new application for this phenomenon was reported: the focusing of a laser beam due to the photorefractive effect. [2]

Doped Crystals

Figure 1 shows a simplified model of the energy levels in a crystal. The valence band is separated from the conduction band by an energy difference of approximately 4 eV, which is referred to as the Band Gap of the material. When electrons are excited from the valence band to the conduction band, they are free to migrate anywhere in the crystal. Because the energy gap is about 4 eV, it would take an ultraviolet photon to excite an electron from the valence band into the conduction band. Ultraviolet light is not a desirable optical source due to the harmful nature of ultraviolet light. This problem can be solved by adding impurities, dopants, in the crystal while it is grown. The dopants provide energy levels within the energy gap. With doped materials, it is no longer neces-

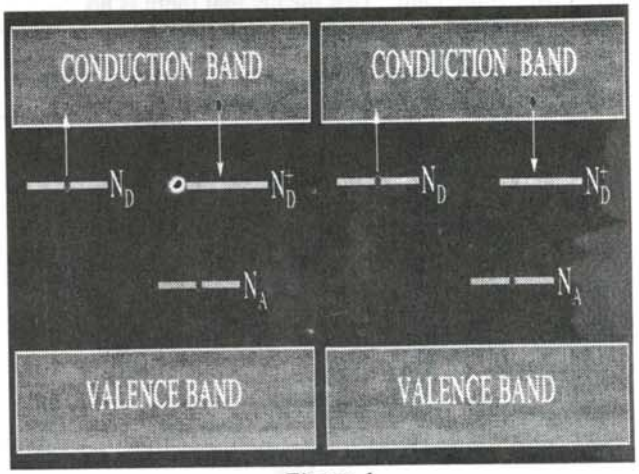

Figure 1
Simplified energy band structure within a photorefractive crystal.

Jeff is a senior computer science student at Northwest Nazarene University. This research was begun while he was a junior engineering physics student. He is currently employed at Itron Inc. in Boise ID. In his spare time, Jeff enjoys playing basketball and taking long walks with his wife Micaela.

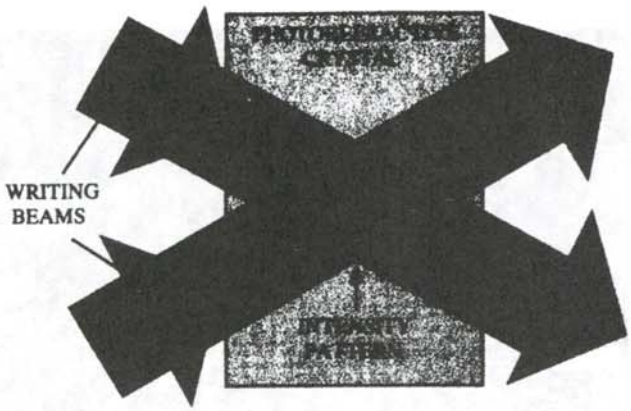

Figure 2
Simplified model for the band transport model, showing two plane waves intersecting within a crystal, producing a modulated intensity pattern

sary to use ultraviolet light to excite electrons from the valence band of the crystal. The energy gap now corresponds to visible light.

There are two types of dopants that are placed in crystals: a number of donor atoms, N_D, and a number of acceptor atoms, N_A. The acceptor atoms have an electron affinity and take an electron from the closest donor atom, making the donor atom which lost the electron an electron trap. This atom is called an electron trap because it will be able to receive electrons from the conduction band should a donor atom (that has not given up an electron to an acceptor atom) release an electron into the conduction band. The number density of traps is N_D^+. This leaves the number density of donor atoms which still retain their original number of electrons, N_D^0:

$$N_D^0 = N_D - N_D^+ . \qquad (1)$$

If, during the formation of the crystal, an acceptor atom acquires an electron, it does not contribute electrons to any process. Consequently, any reactions that occur within the crystal will be between the donor atoms and the electron traps. Since the electron trap has one less electron than a donor atom, it is at a lower energy level. So, if the crystal is excited by photons, an electron from the donor atom will be excited into the conduction band. The electron in the conduction band is free to move due to diffusion and drift. Eventually, it will be captured by an electron trap. When the donor atom gives up its electron, it too becomes an electron trap. This means that the atom would be able to receive an electron from the conduction band. Once the electron trap receives an electron, it can give that electron back into the conduction band.

This phenomenon was modeled in the Band Transport model for photorefraction, first presented in 1976 [3]. Two plane waves intersect in a crystal as shown in Figure 2. These two intersecting waves create a varying intensity pattern within the crystal due to the superposition principle. In the light area, electrons will be excited from the donor atoms into the conduction band, where they will be free to drift and re-trapped and re-excited until they make their way into the dark regions of the crystal. In the dark region, there is a smaller probability of them being re-excited into the conduction band (see Figure 3). Therefore, a relative negative charge will accumulate in the dark regions and a net positive charge in the light regions. This separation of charge between the dark and light regions produces an internal electric field.

This electric field causes a change in the spacing of the atoms in the crystal (known as Pockel's effect). Changing the spacing of the atoms within a crystal results in a small change in the density of the crystal, which changes the speed at which light can propagate through the crystal. If a crystal becomes more dense, the index of refraction increases. If the crystal becomes less dense, the index of refraction decreases. This effect is called the photorefractive effect. The change in index of refraction due to the photorefractive effect is independent of the intensity of the laser beam, as the intensity merely affects the rate at which the charge separation takes place within the crystal, not the size of the electric field caused by the charge separation.

In our experiment, we use a single laser beam incident on the crystal. We assume that the helium-neon laser has a Gaussian intensity profile. Taking the Fourier transform of this Gaussian profile shows it to be synthesized from an infinite number of intersecting plane waves. This means that we have an infinite number of plane wave pairs interacting within the crystal. Each plane wave pair creates a change in the index of refraction of the crystal via the photorefractive effect. Since all of the plane wave pair interactions are taking place at nearly the same place within the crystal, the net effect is that the crystal adds up all of the index of refraction changes.

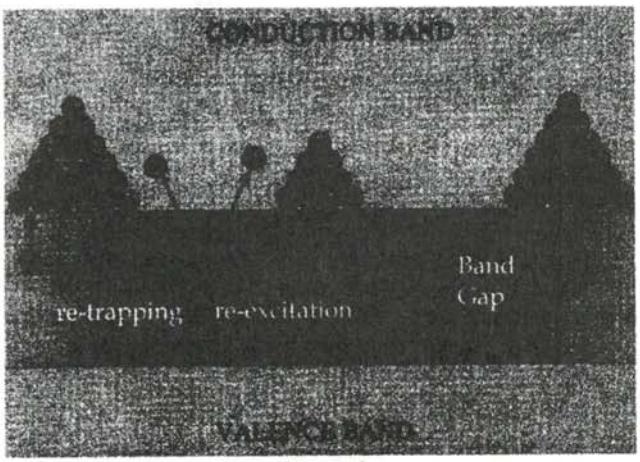

Figure 3
Simplified picture of the electron redistribution within a photorefractive crystal.

Mathematical Model

Coordinate system

The c-axis of the crystal, the direction of the original poling field of the crystal, is defined as the positive x-direction. The laser beam propagates in the positive z-direction. The two plane waves which intersect within the crystal are monochromatic and have amplitudes a_1 and a_2, polarization states p_1 and p_2 and wave vectors $\vec{k}_1$ and $\vec{k}_2$. The intersecting plane waves produce a modulated intensity pattern with a grating wave vector:

$$\vec{k}_g = \vec{k}_1 - \vec{k}_2 \ . \tag{2}$$

The intensity of the pattern is proportional to the square of the resultant electric field at that point. To simplify our model, the bisectrix angle between the two intersecting plane waves is parallel to the z-axis of the crystal, making the grating wave vector:

$$\vec{k}_g = k_g \hat{x} \ . \tag{3}$$

Rate Equation

The rate of change of the density of ionized donor atoms (neglecting thermal ionization) is the difference between the rate at which donor atoms are excited and the rate at which ionized donor atoms recapture electrons from the conduction band:

$$\frac{\partial N_D^+}{\partial t} = s\, I(x)\, (N_D - N_D^+) \ - \gamma_R\, n_e\, N_D^+ \ , \tag{4}$$

where s is the photoionization cross-section, $I(x)$ is the incident intensity distribution along the x-axis, γ_R is the recombination coefficient of a free electron at the site of an ionized donor and n_e is the density of electrons in the conduction band.

Current Density

The current density, j_x, is the current per unit area perpendicular to the flow of the current within a volume. In our simplified model, it contains drift and diffusion terms:

$$j_x = q_e\, \mu_e\, n_e\, E_x + \mu_e\, k_B\, T \frac{dn_e}{dx} \ , \tag{5}$$

where q_e is the magnitude of the charge of the electron, μ_e is the electron mobility, E_x the total electric field (the sum of the internal field and any externally applied electric field), k_B is Boltzmann's constant and T the absolute temperature.

Continuity Equation

Any spatial variation of the current density must be accompanied by the accumulation or depletion of charge carriers in the region of variation:

$$\frac{\partial j_x}{\partial x} = - q_e \frac{\partial}{\partial t}\left(N_D^+ - n_e\right) . \tag{6}$$

Gauss' Law

The spatial variation of the electric field is dependent on the charge distribution in the material:

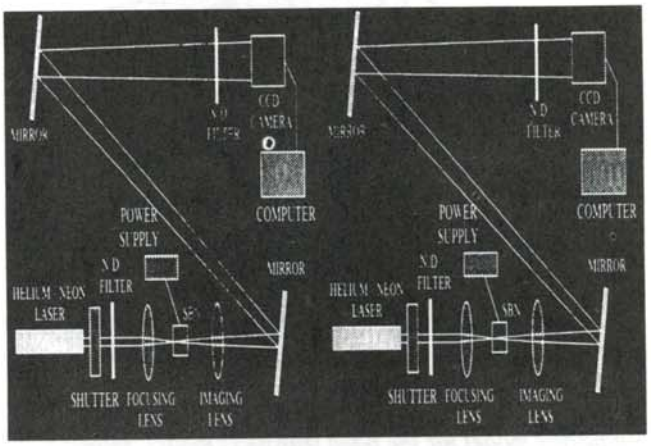

Figure 4
Schematic diagram of the experimental apparatus used for the observation of the photorefractive defocusing.

$$\frac{\partial E_x}{\partial x} = \frac{q_e}{\varepsilon}\left(N_D^+ - n_e \ - N_A\right) . \tag{7}$$

where ε is the static permittivity of the material.

In our model, the redistribution of charge produces an electric field as described by Equation 7. The field distorts the crystalline lattice, producing an index of refraction change Δn, given by:

$$\Delta n = -\frac{1}{2}\, n_o^{\,3}\, r_{eff}\, E \ , \tag{8}$$

where n_o represents the zero-field index of refraction of the crystal, r_{eff} is a linear combination of elements of the linear electro-optic tensor that depends both on the orientation of the crystal and the direction of the externally applied electric field, and E is the total field in the crystal.

Defocusing

We apply a 'negative' voltage (antiparallel to the original poling field) across the crystal. This produces a negative change in the index of refraction of the crystal which reduces the index of refraction. The magnitude of the change in index of refraction is highest at the center of the beam. This causes the crystal to behave in a fashion similar to that of a concave lens, causing the laser beam profile to expand as it propagates through the crystal. The magnitude of the applied voltage determines the magnitude of the change in the index of refraction and consequently, the degree of defocusing.

APPARATUS

Figure 4 is a schematic representation of the experimental apparatus. A 10 mW helium-neon laser, mounted on an optical table, was incident on an 6 x 6 x 6 mm strontium barium niobate (SBN:60) crystal that was doped with 0.016 percent by weight molybdenum and chromium and an unknown amount of triply ionized iron. The crystal was poled in an 8kV/cm electric field. The shutter and neutral density filters were used to control the intensity of the laser beam incident on the crystal. The beam profile

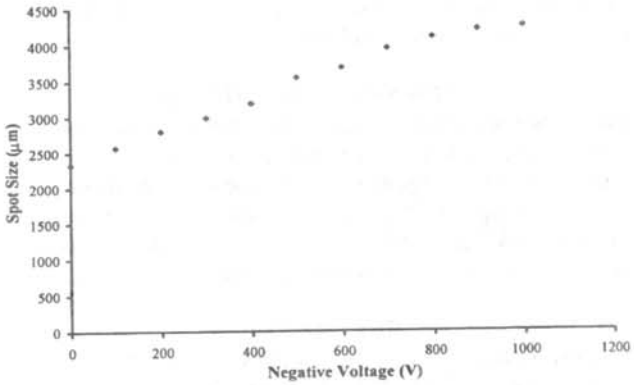

Figure 5
Minimum beam spot size at the exit face as a function of the externally applied voltage. Notice the direct relationship between the spot size and the voltage.

was measured using a CCD camera and SPIRICON beam profile software.

A focusing lens, placed between the neutral density filters and the crystal, reduced the size of the beam within the crystal by placing the waist of the laser beam at the entrance face of the crystal. This reduction in size limits the amount of asymmetric scattering within the crystal.

Silver electrodes covered two opposite faces perpendicular to the poling direction of the crystal. They allowed for an electric field to be applied evenly across the crystal, much in the same manner as a in parallel plate capacitor.

An important aspect of this experiment is to monitor the dimensions and intensity of the laser beam as it propagated through the crystal and after it exited the crystal. To accomplish this, an adjustable imaging system was devised. A mechanical driven shutter allows discrete pulses of light to hit the crystal. The amount of energy striking the crystal was controlled so that the photorefractive effect would not take place too fast for data to be collected.

After exiting the crystal, the laser beam strikes an imaging lens. This imaging lens is mounted on a micrometer, allowing adjustment of the image plane of the camera within and beyond the crystal.

To redo experiments, the index of refraction change must be erased. This change can be destroyed by shining polychromatic incoherent light on the crystal. The white light excites the electrons through the crystal into the conduction band. Once there, the electrons are free to move due to Coulombic repulsion and drift. Eventually they uniformly disperse themselves within the crystal. This basically eliminated the space charge field and the resultant change in index of refraction that is caused by the photorefractive effect. Before each data run, we exposed the crystal to incoherent white light.

PROCEDURE

Two types of data were collected during this experiment: temporal runs and spatial runs. In a temporal run, the evolution of the spot sized viewed at the exit face of the crystal was monitored over a period of time. In a spatial run, the spot size of the laser at different planes along the z-axis of the crystal was observed during a time interval of 3 -5 ms during the maximum defocsing period.

To locate the entrance face of the crystal, a 100 micron pinhole was placed on the entrance face of the crystal. The imaging system was adjusted until the pinhole was imaged clearly. To locate the exit face of the crystal, the same pinhole was placed on the exit face of the crystal and the imaging system adjusted until the pinhole focused clearly. The positions of both the entrance and exit face of the crystal were recorded and used to set up the experimental apparatus for both the temporal and spatial data runs.

After the faces of the crystal were located, the erase light (incoherent white light) was focused into the crystal for 15 minutes to erase any gratings that were within the crystal. A voltage at which to take data was chosen and the imaging system position to image the exit face of the crystal. A temporal data run was then done, recording the spot size as a function of time. The time at which maximum defocusing took place was determined. This was the time at which to perform the spatial data run at that specific voltage. The laser spot size was recorded as a function of position beginning at the entrance face of the crystal and continuing past the exit face of the crystal.

RESULTS

Figure 5 shows the spot size at the exit face of the crystal as a function of the voltage applied across the crystal. The increasing spot size shows that the crystal is acting as a defocusing lens. Figure 6 shows the spot size at the exit face of the crystal as a function of the time that the voltage

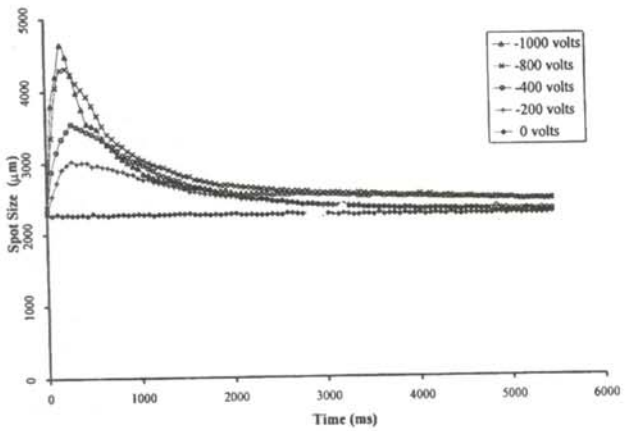

Figure 6
Beam spot size at the exit face of the crystal as a function of time for different externally applied voltages.

has been applied across the crystal face. Data were also taken at different imaging locations inside the crystal. These results show that there is a defocusing taking place within the crystal which is directly related to the magnitude of the applied voltage

The data from this experiment indicate that the SBN:60 crystal can be made to behave as a variable focal length defocusing lens. The magnitude of the defocusing is directly related to the size of the voltage applied across the crystal. As the voltage increases, the time necessary for the maximum defocusing to occur decreased. This effect can be understood by examining the motion of the electrons in the combined charge-separation induced and external fields. The larger electric field accelerates the drifting electrons in the conduction band at a greater rate, causing them to move into the dark region faster than at larger voltages.

As the laser and external voltage continue to be applied to the crystal, the electrons will move in the opposite direction of the externally applied electric field. This overall motion will continue until the separation of charge within the crystal creates an internal electric field which is equal and opposite to the externally applied electric field. This internal electric field 'screens' the external electric field and causes the defocusing due to the photorefractive effect to vanish as seen in Figure 6.

ACKNOWLEDGMENTS

The author would like to thank Dr. Duree for the opportunity to conduct this research project with him and for his insight and encouragement. This research was made possible in part by grants from the Research Corporation, the Murdock Charitable Trust Foundation and the Science and Math Associates of Northwest Nazarene College.

REFERENCES

* Current address of author: Jeffrey Blum, 908 Locust St. #E2, Nampa, ID 83686 Blumer@Hotmail.com

1. F.S. Chen, J. Appl. Phys., 38, (1967), p. 3418.
2. G.C. Duree, Jr., Phys. Rev. Lett., 71, (1993), p. 533-536.
3. N.V. Kukhtarev, Sov. Tech. Phys. Lett., 2, (1976), p. 1114-1119.

FACULTY SPONSOR

Dr. Galen C. Duree Jr.
Physics Department
Northwest Nazarene College
Nampa, ID 83638
gcduree@science.nnc.edu

MODAL ANALYSIS OF PERCUSSION INSTRUMENTS USING VIBRATIONAL HOLOGRAPHY

Robert Bedford *
Department of Physics
Stetson University
DeLand, FL 32720
received September 1, 1998

ABSTRACT

Many musical instruments, including numerous percussion instruments, rely on sounds produced from vibrating plates. Using vibrational holography, we gained very accurate information about the patterns of vibrations (modes) of these plates. Time-average vibrational holography uses two beams of coherent light that interfere on high-resolution holographic film. One beam, with a fixed path length, is used as a reference beam, while the object beam is incident on the vibrating plate. The vibrating plate changes the path length of the object beam to create interference rings about the antinodes of vibration We examine the motion of a G_3 hand bell and compare it with the modes of a circular plate. Measurements of the same mode at several different driving amplitudes yield holographic data comparing well with theoretical amplitude calculations.

INTRODUCTION

All sounds can be thought of as a superposition of pure sine waves. When an object vibrates at multiple frequencies, the motion becomes complex and no longer appear to be sinusoidal. We know now that the sound waves produced by the complicated motion can be broken up into several sine waves with distinct frequencies and amplitudes using Fourier transform. These decompositions are called the modes of oscillation of the system. The study of the different modes of vibration is useful in areas such as musical instrument manufacturing and evaluating turbine performance.

Chladni Plates

Ernst Chlandi was the first to study these modes in 1787.[1] Chlandi used uniform flat plates bowed on edge, forcing them into oscillation to study the vibrational behavior of flat surfaces. Due to the relatively small amplitudes of oscillation, it is difficult to analyze the modal behavior of such surfaces. Chladni studied the modes by placing sand or fine shavings on the driven plate. The sand moves to the lines on the plate that do not vibrate, called nodal lines. The resulting plate with sand lines at the nodes of vibration of the plate gives a good picture of the modes of vibration of the plate. The various modes resonate with specific frequencies that depend on the material of the plate as well as its shape and thickness. The mode is identified by the notation (n,m), the number of nodal diameters, n, and the number of nodal circles, m. This technique relies on the assumption that the sand is massless and moves with little force applied to it and is limited by the fact that the surface must be relatively horizontal and relatively flat.

A much more sensitive and versatile way of analyzing the modes is to use vibration holography or holographic interferometry. Most notably, Thomas Rossing has made significant contributions to the field, specifically examining musical instruments. [2] First proposed by Stetson and Powell in 1965 [3], vibrational holography applies what we know of optics and wave superposition to study the vibrational modes. An interference pattern is produced by the superposition of a reference beam and object beam to show the nodal and antinodal areas of the plate. Figure 1 shows a uniform circular plate vibrating in nodal diameters and notal circles in a (3,1) configuration. To guarantee coherence, a single 5mW He-Ne laser beam is split to provide both the reference beam and object beams. The object beam interacts with an object that is driven at a

This research began in the summer before Robert's senior year at Stetson University. He is now working as a Ph.D. candidate at the Optical Sciences Center of the University of Arizona. He is working with grating coupled semiconductor unstable resonators. In his free time, Robert enjoys hiking and bike riding in southern Arizona's mountains.

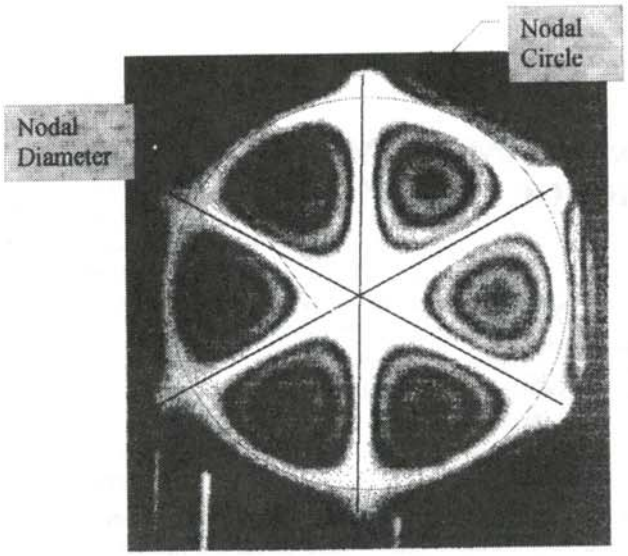

Figure 1
Vibrational holographic image of a uniform plate. There are e nodal diameters and 1 nodal circles. Lines have been drawn in to identify the nodal lines and circles of the plate.

particular frequency by a small mass driving magnet and an driving coil. The laser light reflected by the object beam interferes with the reference beam on an emulsion as shown in Figure 2.

In a standard hologram, the object is not vibrating. In this case, there will be interference at many different places on the film due to the difference in path traveled by the reference beam and the beam reflecting off the non-regular shape of the object. The interference from the path differences creates a complex diffraction pattern on the film. Once we develop the holographic film, the areas of constructive interference become spots on the film. When we us the same laser to view the image, the complicated

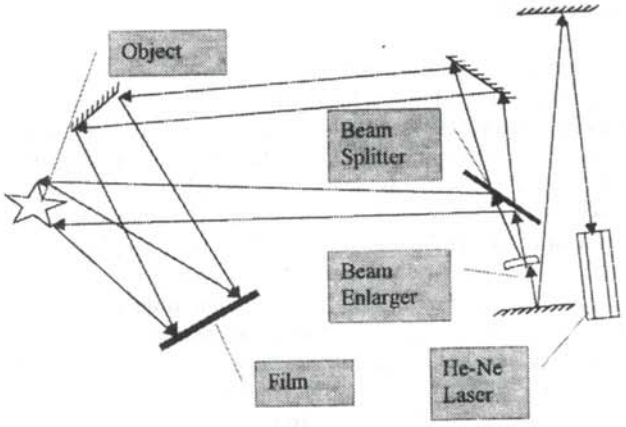

Figure 2
Schematic diagram of a holography setup.

spot pattern diffracts the reference beam to form a virtual image of the object.

When the object is vibrating in a sinusoidal manner, it spends most of its time at the point of maximum displacement as there the velocity is zero, keeping the object at the same displacement. The interference pattern created when the vibrating object is at the positive and negative maximum displacements will emphasize certain areas in the grid of the points of interference on the film. While the plate is moving between the positive and negative amplitudes, the interference pattern on the film is average out in time and consequently does not significantly add to the diffraction pattern. The surface only has to move one half a wavelength of the illuminating light to change the pattern from constructive to destructive. [4] This is commonly referred to as 'one dark fringe of vibration'. Because the wavelength of the laser, 632.8 nm, is very small, the spatial resolution is excellent at low amplitudes of oscillation of the object. The fringes get closer together when the path difference increases. A bulls-eye pattern is created when an antinode is located. [5]

THE HOLOGRAM

First, let us consider a single exposure hologram. The electric field incident on the holographic film is the vector addition of the fields, the reference beam:

$$E_{ref} = r\, e^{i\omega t}\, e^{i\frac{2\pi}{\lambda} x \sin(\alpha)} \quad (1)$$

and the object beam:

$$E_{obj} = s\, e^{i\omega t}\, e^{i\frac{2\pi}{\lambda} x \sin(\beta)}, \quad (2)$$

where r and s are the amplitudes of the waves, α is the phase change due to the location of the reference beam, β is the phase change do to the place on the object where the object beam reflected and λ is the wavelength of the illumination light. The total field at the plate is:

$$E_{total} = E_{obj} + E_{ref} = s\, e^{i\omega t}\, e^{i\frac{2\pi}{\lambda} x \sin(\beta)} + r\, e^{i\omega t}\, e^{i\frac{2\pi}{\lambda} x \sin(\alpha)}. \quad (3)$$

What gets recorded on the film is the intensity:

$$I = E_{total}\, E_{total}^{*}. \quad (4)$$

Substituting Equation 2 and 3 into Equation 4 gives.

$$I = r^2 + s^2 + E_{obj}\, E_{ref}^{*} + E_{ref}\, E_{obj}^{*}. \quad (5)$$

Substituting in Equations 1 and 2 gives:

$$I = r^2 + s^2 + rs\, e^{i\left[\frac{2\pi}{\lambda} x \sin(\alpha) - \frac{2\pi}{\lambda} x \sin(\beta)\right]} + rs\, e^{-i\left[\frac{2\pi}{\lambda} x \sin(\alpha) - \frac{2\pi}{\lambda} x \sin(\beta)\right]}. \quad (6)$$

Illuminating the film with the reference beam results in:

$$E_{res} = \left(r^2 + s^2\right)E_{res} + r^2 s\, e^{i\left[\omega t + \frac{2\pi}{\lambda} x \sin(\alpha)\right]} + r^2 s\, e^{i\frac{2\pi}{\lambda} x \sin(\beta)} e^{i\left[\omega t + \frac{2\pi}{\lambda} x \sin(\alpha)\right]}, \quad (7)$$

the re-illumination beam attenuated as it passes through the holography film. The first term in Equation 7 is actually the reference beam, modulated in amplitude but not phase. This means that the incident beam passes through the film unchanged. The second term in Equation 7 describes the electric field that would come from the

object. The third term in Equation 7 is the electric field due to a real image of the object, but is not important in our experiment.

The phase of the second term in is only for a stationary object. If must consider a time dependent optical path difference, Δ. If the unit vector $\hat{n}_1$ is the direction of the illumination of the object, $\hat{n}_2$ the direction to the film and $\hat{n}_m$ the direction of the vibration, then the optical path difference is given by:

$$\Delta = A(\vec{r},t)\,\hat{n}_m\cdot\left(\hat{n}_1 + \hat{n}_2\right), \tag{8}$$

where $A(\vec{r},t)$ is the displacement, $\vec{r}$, at any particular point on the object. If $A(\vec{r},t)$ is a sinusoidal function of time represented by:

$$A(\vec{r},t) = A(\vec{r})\sin(\omega t), \tag{9}$$

where ω is the angular frequency, the image field is given by:

$$E_{image} = E_o\, e^{i\frac{2\pi}{\lambda}A\,\hat{n}_m\cdot\left(\hat{n}_1+\hat{n}_2\right)\sin(\omega t)}, \tag{10}$$

where E_o is a function varying with time as:

$$E_o = r^2 s\, e^{i\omega t}. \tag{11}$$

If we take the time average of Equation 10

$$\left\langle E_{image}\right\rangle = E_o\,\frac{1}{T}\int_0^T e^{i\frac{2\pi}{\lambda}A\,\hat{n}_m\cdot\left(\hat{n}_1+\hat{n}_2\right)\sin(\omega t)}dt\,. \tag{12}$$

The resulting image has an irradiance that goes as a zero order Bessel's function perpendicular to the nodes of vibration: [7]

$$I = \left|E_o\right|^2\left|J_o\left(\frac{2\pi}{\lambda}A\,\hat{n}_m\cdot\left(\hat{n}_1+\hat{n}_2\right)\right)\right|^2 \tag{13}$$

Equation 12 is the intensity of a single point on our object, but can be used to describe any of the points on our object. Since every point on the object acts as a single source, it is possible to sum (or integrate) over all points to reconstruct the object.

THE EXPERIMENT

A small mass magnet is attached to vibrate the object we wish to analyze. This magnet is placed in a driving coil supplied with a sinusoidal voltage signal. The magnet responds to the field produced by the coil to force the object to vibrate at the specified frequency.

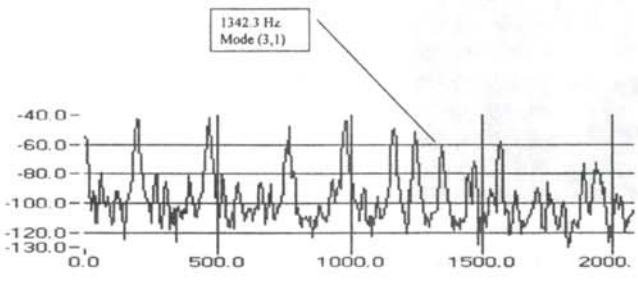

Figure 3
Power spectrum of a G_3 hand bell being driven with pseudorandom noise. The (3,1) mode discussed in this paper is marked at 1342 Hz.

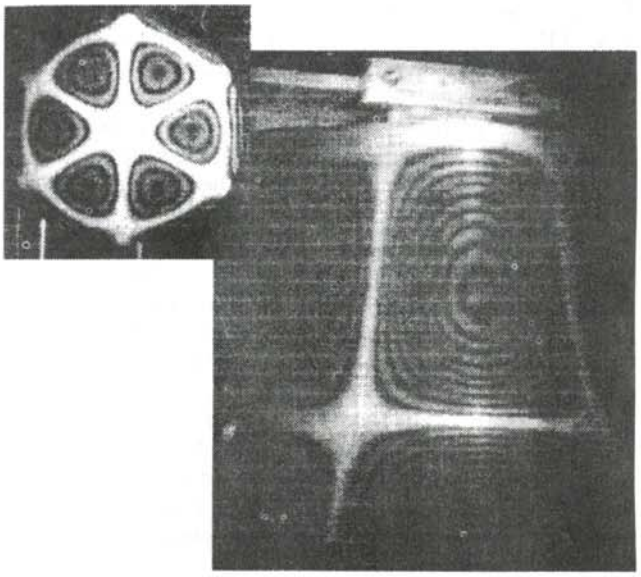

Figure 4
Comparison of a (3,1) mode of the hand bell to that of a flat plate. Note the similarities.

We first drive the object with a pseudorandom noise generator to get a Bode power spectrum, log(power) vs frequency. An example is shown in Figure 3. This is useful as the standing modes of the object will vibrate and can be identified using a near field microphone. Once we have found the resonant characteristics of the object, we use the attached magnet and drive coil to sinusoidally drive the object at a constant amplitude at the chosen frequencies.

For time-average vibrational holography, the only exposure requirement is that it span over many periods of vibration of the object. One second or less is appropriate for vibration frequencies in the audible range (20 Hz - 20 kHz), but the film sensitivity and laser power limit practical exposure times. A typical exposure time for our system was on the order of 2 minutes.

G_3 Hand Bell

A hand bell does not appear to be an object that acts like a flat plate, but, with some imagination, one can make a reasonable comparison. If we unfold the bell such that the handle is at the center of the newly formed disk, the hand bell appears similar to a round flat plate. This similarity is shown in the vibrational holography results shown in Figure 4. The hand bell, however, does have some unique attributes that have interested musicians.

The amplitudes of vibration of the hand bell can be measured using vibrational holography.7 The (3,1) mode of the hand bell at two different amplitudes are shown in

Figure 5. Both show the bell driven at a frequency of 1342.3 Hz. The nodal lines and circles are in the same places, showing us that both pictures are of the same mode. The relative displacement can be determined by counting the number of fringes in each of the pictures. If the interference is assumed to be linear, the ratio of the amplitudes is the same as the ratio of the fringes. In Figure 4b there are 9.5 fringes and in Figure 4a, there are 3.5 fringes. The ratio is 2.71. A better approximation for the relative amplitudes is to assume that the fringes are caused by the Bessel function in Equation 13. Using a table for zeros for Bessel functions we can find the ratio of the displacements to be 1.46/0.514 = 2.85.

We check these results by measuring the intensity of the sound waves produced by the bells and the same driving amplitudes and frequencies as were used for the vibrational holography runs. The intensities, recorded in dB, were measured using a near field microphone. We can use the relative sound intensity level (SIL) measurements to determine the relative amplitudes:

$$SIL_2 - SIL_1 = 10\log\left[\frac{I_2}{I_o}\right] - 10\log\left[\frac{I_1}{I_o}\right] = 10\log\left[\frac{I_2}{I_1}\right]$$
$$= 10\log\left[\frac{(d_2)^2}{(d_1)^2}\right] = 20\log\left[\frac{d_2}{d_1}\right], \qquad (14)$$

where I_o is an arbitrary reference intensity and d_i is the amplitude of motion. The sound level measurements give is an amplitude ratio of 3.16. This value is within 10% of the holographic values. The vibrational holography appears to be a successful technique for measuring the movement of complicated surfaces at the antinodes.

ACKNOWLEDGMENTS

The author would like to thank Dr. Kevin Riggs for the wide range of knowledge and time resources devoted to vibrational holography. He also thanks Larry Ramsey for being able to fabricate outstanding mounts and research tools.

REFERENCES

* Current address of the author: 3121 N. Swan Road, Apt 137, Tuscon, AZ 85712 Bedfordr@optics.Arizona.Edu

1. E.F.F. Chlandi, "Entdeckungen über die Theorie des Klanges", translated excerpts in R.B. Lindsay, Acoustics: Historical and Philosophical Development, Hutchinson and Ross, Stroudsburg, PA, (1973).
2. T.D. Rossing, R. Perrin and H.J. Stahoff, et.al., "Vibrational Modes of Tuned Handbells", Journal of the Optical Society of American, 55,12, (1965), pp. 1593-1598.
4. S.M. Khanna, J. Tonndorf, et. al., "Vibratory Patterns Examined by Real-Time and Time-Averaged Holography", Journal of the Acoustical Society of America, 54, 6, (1973), p. 1686-1693.
5. J. Hansberger, K. Johnson, A. Larson, S Pankratz, T. Ramsland, J. Sheard, T. Smith, "Time Averaged and Real-Time Holographic Interferometry of a Resonating Hand Bell", Bethel College Optics Student Paper, Spring 1992.
6. G.M. Brown, R.M. Grant, et. al. "Theory of Holographic Interferometry", Journal of the Acoustical Society of America, 45, 5 (1969), p. 1166-1179.
7. R.L. Powell, K.A. Stetson, "Interferometric Vibration Analysis by Wavefront Reconstruction", Journal of the Optical Society of America, 55, 12 pp.1593-1598.

FACULTY SPONSOR

Dr. Kevin Riggs
Department of Physics
421 N Woodland Blvd, Unit 8267
Stetson University
DeLand, FL 32720-3756
physics@stetson.edu

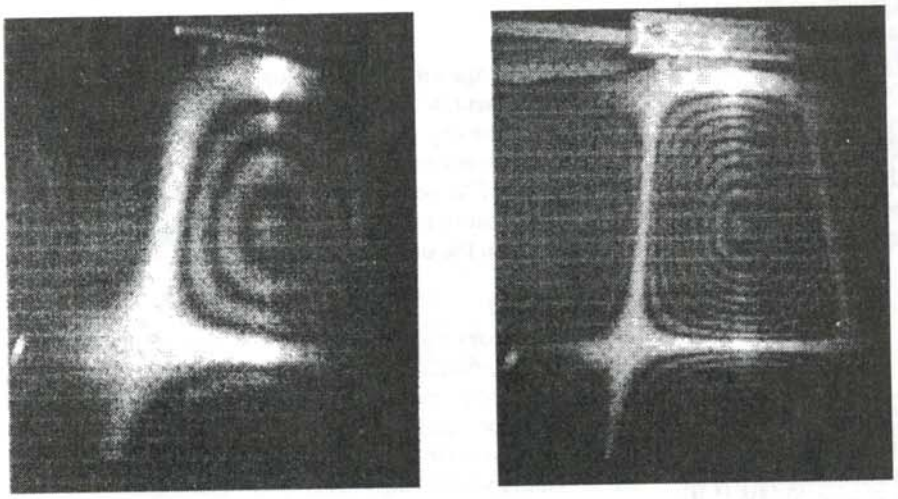

Figure 5

Two vibrational holograms of the G_3 hand bell driven at different amplitudes. a) (3,1) mode driven at -60.2 dB. b) (3.1) mode driven at -50.0 dB. Examining the modal lines shows there are 3.5 dark fringes (if we count the light center of the bulls-eye at a half) on the left hologram and there are 9.5 dark fringes on the hologram driven at a larger amplitude.

EXPLORATION IN TEN PIN: A SIMPLIFIED MODEL OF A BOWLING SYSTEM

Jocelyn Christensen*
Department of Physics and Astronomy
Carleton College
Northfield, MN 55057-4025
received December 14, 1998

ABSTRACT

The complicated physical system of bowling is simplified to a two-dimensional model, where the pins and ball are represented by hard disks, friction is neglected and straight line motion and elastic collisions are assumed. We show that, while not entirely realistic, the model reflects some of the behavior we see occurring in a real, three-dimensional bowling system. This simplified model reveals tremendous sensitivity to the initial parameters of the system and provides insight into the nature and dependence of the elusive strike zone.

INTRODUCTION

The game of bowling uses a complicated physical system. If all of the factors that affect the system in reality were taken into consideration, a mathematical representation of the system would be nearly impossible to develop. The list of factors that realistically complicate the system is large: spin on the ball, the toppling and rolling effect of the oddly shaped pins, the inelastic nature of collisions... [1] Countless bowlers, from novice to professional, have at some point in their careers wondered, when it seems as though the ball travels repeatedly with the same speed along the same path, why that sometimes a strike occurs and sometimes 2 or 3 pins are left standing. The large number of physical factors that complicate the system seem to be the cause of the inherent unpredictably and seeming irreproducibility of the bowling system. In this paper, we will strip away many of the complicating factors and examine the bowling system in an idealized form.

Jocelyn is a senior math major at Carleton College. This research was done in the summer of her sophomore year, when she interned with the amiable and supportive Carleton College physics department. She is currently considering graduate schools in architecture and theater, although she loves writing and may pursue a career in journalism. When she does get a job, she hopes she can ride her bike to work. Jocelyn has a passion for Shakespeare, and is often distracted from problem sets by daydreams of playing Juliet, Lady Anne, Ophelia or Lady MacBeth.

There are a number of fixed parameters in the bowling game. These come directly from standards set by the American Bowling Congress (ABC).[2] The pins are arranged in the shape of an equilateral triangle and are numbered from 1 to 10. By convention, the head pin is numbered 1. The numbering continues back row by row, increasing in value from left to right. The pins are 1 foot apart, measured from center to center. The largest circumference of the pin is 0.20 feet (or 2.5 inches). The bowling ball has a radius of 0.36 feet (4.3 inches) and can weight from 9 pounds to 16 pounds. According to ABC regulations, the pins must weigh between 2 pounds 14 ounces and 3 pounds 4 ounces. The alley is 3.5 feet across. The distance from the center of the head pin to the back pit is 3.0 feet.

THE MODEL

Assumptions

We assume a frictionless level plane as the alley. The ball and pins are represented by two-dimensional disks. Collisions are assumed to be completely elastic. Between collisions, the disks move in straight lines. These assumptions mean that in our model, unlike in a real bowling system, the outcome is independent of the initial speed of the ball. In spite of this featu:. the essence of the bowing system is preserved.

In our simulation, we only consider the cases where initially all 10 pins are standing and where the first collision occurs between the ball and the head pin. Considering other situations would illuminate the other bowling phenomena, but our interest lies in exploring the nature of strikes (where all 10 pins fall).

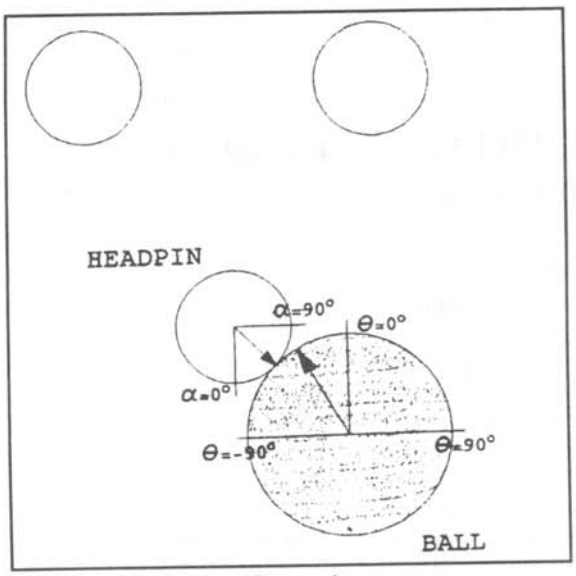

Figure 1

Conventions used to describe the ball's initial position, α, and the angle of the initial velocity of the ball, θ. There the ball is at position α = 45° with a velocity represented by the arrow in the ball, θ = 30°

Parameters

The relevant parameters fall into two categories: those that have fixed values and those that can be varied. The fixed parameters are the physical arrangement of the pins, the radii of the pins, the radius of the ball and the location of the edges of the alley (all specified by the ABC). The parameters that can be varied are the initial point of contact between the ball and the head pin, the angle of the initial velocity of the ball and the ball to pin mass ratio.

The dimensions of the alley are used as boundary lines in our system. When a disk goes beyond these lines, it no longer participates in the collision action. In reality, a pin has the opportunity to bounce off the sides of the alley and re-enter the system, but in our model, this is not allowed.

We define the variable parameters in terms of two distinct Cartesian axes, imposed on the ball and on the arrangement of the pins as shown in Figure 1. The initial contact point is determined by the angle, α, of the line connecting the contact point and the center of the head-pin, shown in Figure 1 as the arrow pointing towards the ball. The point closest to the bowler on the circumference of the head pin corresponds to $\alpha = 0^\circ$. The direction of the initial velocity of the ball is the angle θ. When the velocity of ball has no sideways component, we say that $\theta = 0^\circ$. Values of α range between 0° and 90°, values of θ have a range of 180° perpendicular to the axis of the collision (which turns out be dependent on α). This range includes all possible realistic values of θ and extends to include values that are less possible in a real bowling setting. (For example, some of the combinations have a negative component in the direction of the bowler: back up the bowling alley. Professional bowlers put quite a bit of spin on the ball, which allows for fairly large angles of initial velocity, but it never turns so much that the ball is heading back towards the bowler.)

The final variable parameter is the ball to pin mass ratio, which we call μ. Based on ABC regulations, μ can range from 2.5 to 5.5.

The Simulation

We programmed the simulation in MATHEMATICA™. The algorithm consists of a few steps that are cycled through a number of times until a final condition is met. The initial sate of the system (the program's input) is a list of the position and velocity of the ball and each pin. The ball's velocity is determined by θ and its position by α. The pins are all at rest and set up in their standard triangular formation.

The first step the simulation performs is to look at the initial state and calculate the new velocities of the disks that have collided. This is done simply using the laws of conservation of energy and conservation of momentum, plugging in the mass of the colliding objects as well as their initial positions and velocities. The calculations give the post collision velocities of the objects. This is the post-collision state. The new values are then substituted into the input state in the place of the old velocities. From the positions and velocities of all the pieces, the program calculates for each pair the time it would take for the two particles to collide (if they collide at all). From the list of collision times, the one with the lowest value is selected. The simulation does not allow for the possibility that two collisions could occur simultaneously, because except for the case of a directly centered collision, this would be a highly unlikely occurrence. Because of this feature of the program, the outcome when $\alpha = \theta = 0^\circ$ is disregarded.

Once the program has determined the least collision time, it calculates the position of each particle and replaces the old values with new ones. This is the pre-collision state.

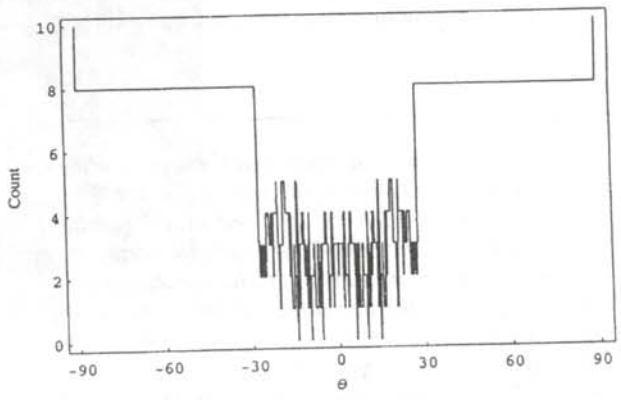

Figure 2

Number of pins remaining vs. the angle of velocity at the collision, θ. Here α = 0° and θ varies by 0.1°.

The pre-collision state then becomes the initial state and the program repeats itself. When the velocities of all the particles are such that no further collisions occur, the program ends, reporting the position and velocity of each particle just after the last collision. This is the final state, which indicates which pins remain standing.

The simulation produces raw data, a list of the position and velocity of each particle after each collision in the system. The first element of the list is the initial state, the last element is the final state. From this information, we can create a static plot, showing the paths of all the particles together without regard to time. The raw data also can be simplified by counting the pins that were never hit. This is the number of pins left standing, and is called the count.

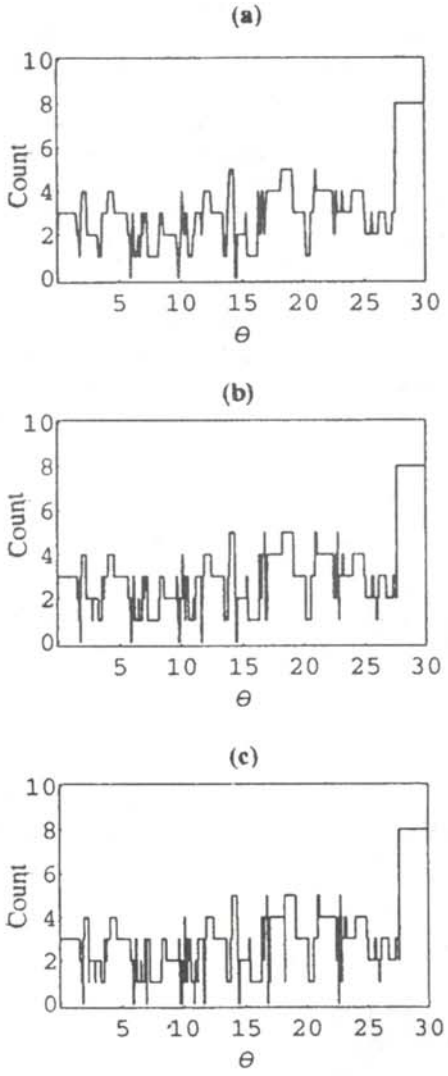

Figure 3
Number of pins remaining vs the angle of initial velocity, q. The count is calculated for θ varying by a) 0.1°, b) 0.01° and c) 0.005°. For each graph α = 0° and μ = 4.

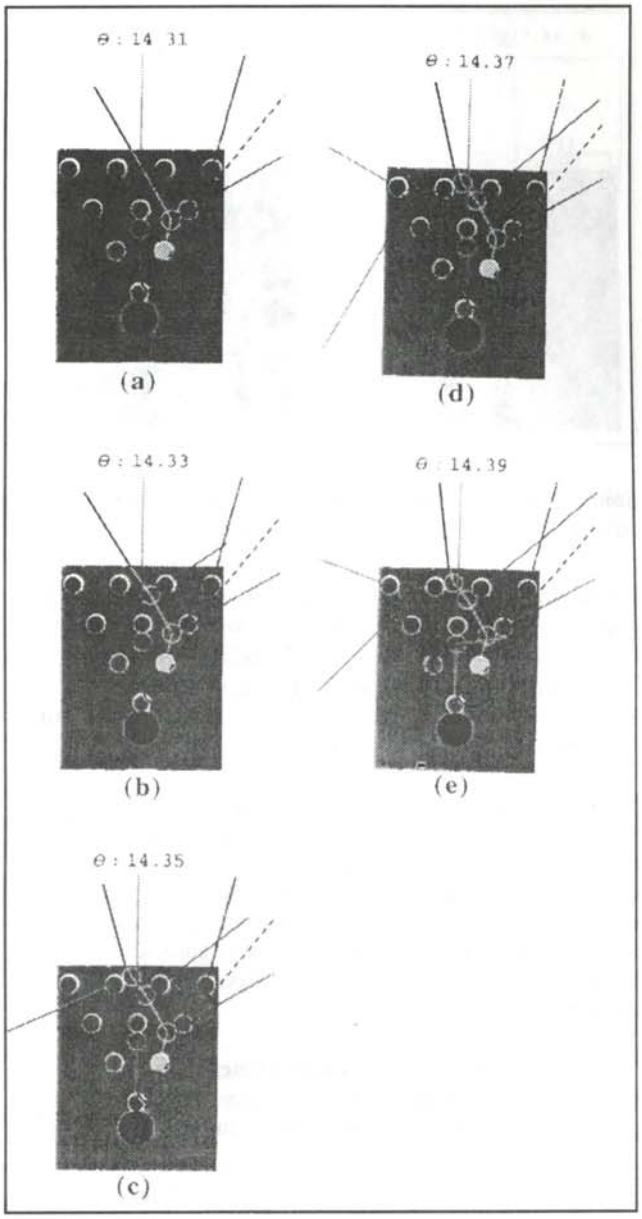

Figure 4
Static plots of the paths of all of the disks for distinct values of θ. Time is not represented in these graphs.

CALCULATION AND DISCUSSION

Sensitivity of the System

Varying the initial velocity

We fixed the initial point of contact between the ball and the head pin to at $\alpha = 0°$, and the mass ratio to at $\mu = 4$ (a moderate mass ratio), and varied the angle of the initial velocity of the ball from $\theta = -90°$ to $+90°$ in discrete increments.

Figure 2 shows the count (number of pins remaining) as θ varies in increments of 0.1 degrees. The graph appears symmetric, which gives us some confidence in the program. The graph shows sharp transitions and a large

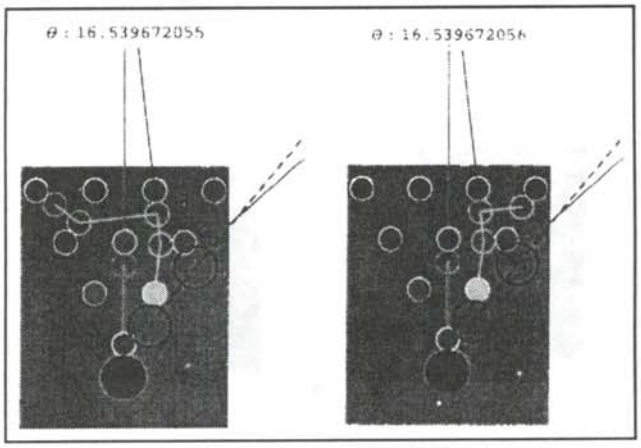

Figure 5
Static plots of the paths of all of the disks for two distinct values of θ which differ by a billionth of a degree.

fluctuation in the number of pins left, even when θ varied only by a fraction of a degree. The wildly fluctuating outcomes raise questions about the behavior of the system. The interesting behavior seems to occur at values of $|\theta|<30^\circ$. Since Figure 2 is symmetric, we restrict our study to θ between 0° and 30°.

Figure 3 shows the results of the simulation with increments of θ of: a) 0.1 degree, b) 0.01 degree and c) 0.005 degrees. Figure 3 shows that increasing the number of data points sampled reveals fluctuation in the system not captured in Figure 2. In Figure 3a, there are only 3 strikes, in Figure 3b there are 5 strikes and in Figure 3c there are ten strikes. This illustrates the sensitive nature of the system to initial conditions.

To understand the interactions that determine such sensitive behavior, we examine in detail the path of the particles where the dramatic fluctuations occur. Figure 4 shows static plots of the paths of all the particle as θ changes from 14.31° to 14.39° in increments of 0.02°. The change in θ seems insignificant, but variations in the behavior of the whole system that result from such small changes in initial conditions are quite apparent. Small changes in the velocity of the ball create more visible changes in the velocity of the 3-pin. These changes make the difference between whether the 3-pin hits just one pin (Figure 4a) or several pins. The same things happens with the pins that the 3-pin hits, they either miss the few pins that remain standing (Figure 4d) or have just the correct velocity to hit them, (Figure 4e).

The manner in which small changes in the initial velocity of the ball affects the behavior of the entire system is illustrated in Figure 5, which shows the resulting paths of the particles as θ is changed by a billionth of a degree. In Figure 5a, the 3-pin hits the 9-pin and heads off in the negative direction (to the left) . In Figure 5b, the 3-pin hits the 9-pin and heads off in the positive direction. In Figure 5a, just before the 3-pin hits the 9-pin, it has a minute negative velocity component (relative to the axis of collision), while in Figure 5b, it has a minute positive position component. There is a single point where the velocity changes from having a negative component to having a positive component, which accounts for the sharp transition in the direction of the velocity of the 3-pin.

Varying the initial point of collision

The same sort of behavior as discussed in the previous section occurs when θ and μ are kept constant and α is varied. The count seems to depend as sensitively on α as it does on θ.

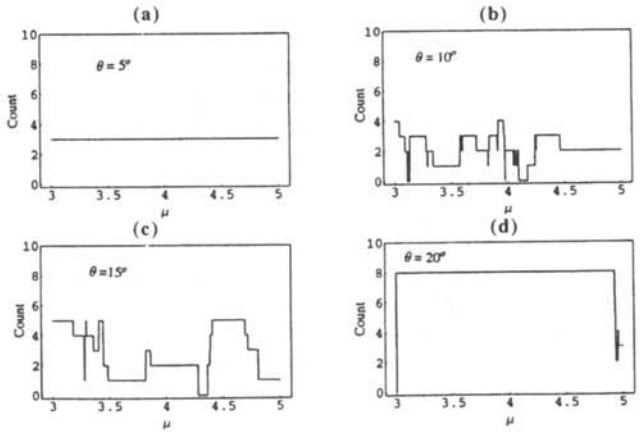

Figure 6
Number of pins remaining vs the mass ratio, μ, for different values of the initial velocity of the ball, θ. In each graph, α = 0°

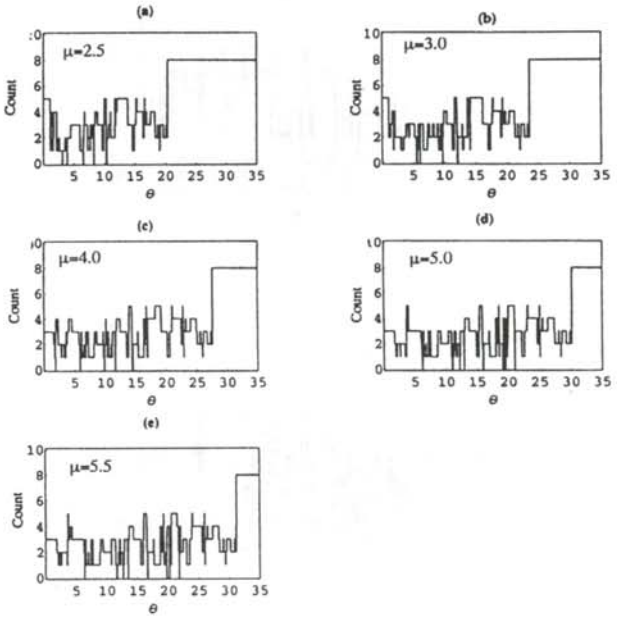

Figure 7
Number of pins remaining vs the angle of the velocity of the ball, θ for different values of the mass ratio, μ. In each graph, α = 0°.

Varying the mass ratio

Variations in μ have a less dramatic influence on the system than variations in α and θ. Figure 6 shows the effects of varying the ball to pin mass ratio for 4 different values of θ. In each case, $\alpha = 0^\circ$. While there is some variation in the outcomes, the fluctuations are not as wild as those seen in the previous results. The results shown in Figure 6a and Figure 6c show that for certain initial angles, the count stays essentially constant as the ball to mass ratio changes.

Professional bowlers typically bowl with a 16 pound ball, the heaviest that the ABC allows. Figure 7 shows the number of pins that remain for $\alpha = 0^\circ$, θ varying as in Figure 2, for 5 different values of μ ranging from 2.5 to 5.5. The structures of each of these graphs are very similar; for larger values of θ, the pattern formed by the fluctuations is the same. There seems to be a point where the count jumps to 8 and remains there for a large range of θ. The value of θ at which this occurs increases with μ. As μ increases, the window of angles within which more than two pins will be knocked down widens. This means that using a heavier ball improves the bowler's change of knocking down at least 2 pins.

The similarity in structure of the 5 sections of Figure 7 explains why when we vary μ as in Figure 6, for some θ values, we see wild fluctuations in the count and for others, the value is constant. On each graph in Figure 7, there are some places where a particular number of pins remain over a significant range of angles, creating a flat line on the graph. These flat ranges would then overlap in graphs of the type in Figure 6, for certain values of θ.

The Quest for the Strike Pocket

Bowlers are perpetually seeking the elusive 'pocket', the small range between the head pin and the 3-pin (for right handers) or between the head pin and the 2-pin (for left handers) that if hit yields strikes. In our model, this pocket

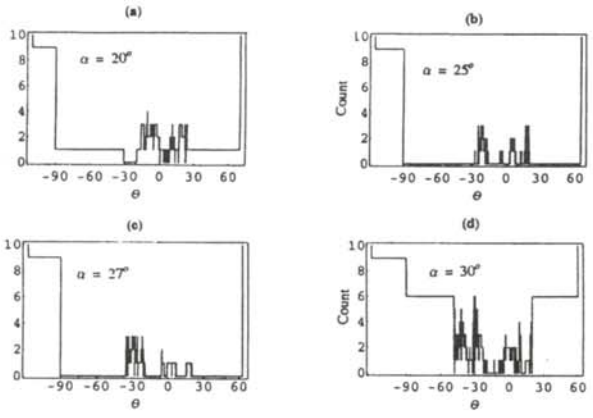

Figure 8

Number of pins remaining vs. the angle of the velocity, θ, for different values of the initial position of the ball, α. For each graph, μ = 4.

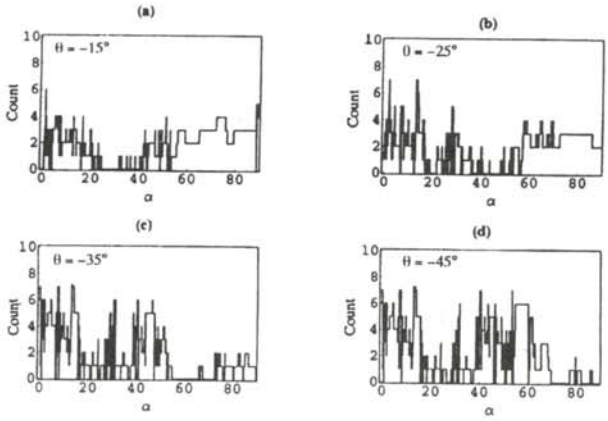

Figure 9

Number of ins remaining vs the initial position of the ball, α for different values of the angle of the initial velocity of the ball, θ. For each graph, μ = 4.

is dependent on a combination of the angles α and θ.

We search for this 'pocket' by holding α constant and varying θ. Recall that Figure 2 shows the effects of varying θ at the fixed position $\alpha = 0$. Figure 8 shows the effect of varying θ through 180° for several different values of α. These figures show that although the possibility for getting a strike exists at many values of α, at certain initial contact points, there are larger ranges of θ which will yield strikes. In Figure 2, there are only a few isolated values of θ that result in a strike (count of zero). In contrast, Figure 8a shows a count of zero for the range of θ values from about -30° to -20°. This is the first suggestion of what might be called a 'strike zone'. In Figure 8b, we see much more impressive results. At a position of $\alpha = 25^\circ$, any θ value in the range from -30° to +30° will yield a strike. Figure 8c , where $\alpha = 27^\circ$, shows much the same effect. At a position of $\alpha = 30^\circ$, as illustrated in Figure 8d, the chance of getting a strike again becomes less probable. Even though at $\alpha = 25^\circ$ and $\alpha = 27^\circ$ there are large ranges of θ at which strikes occur, there are variations within those ranges where some pins are left. These data show that the outcome of the bowling system is sensitively dependent on both the initial velocity of the ball and the location of the initial point of contact.

The 'pocket' with regard to the initial point of contact

In contrast to Figure 8 where α was held constant and θ varied, Figure 9 shows the effect of varying α from 0° to 90° for several different fixed values of θ. In Figure 9 it is much more difficult to pinpoint a significant range of α that consistently yields strikes. There appears in Figure 9 a trend in the values of α that correspond to the most strikes. In Figure 9a, $\theta = -15^\circ$, the most concentrated range of strikes occurs in the range $\alpha = 20^\circ$ to $\alpha = 40^\circ$. In Figure 9b, where $\theta = -25^\circ$, the concentrated ranges of strikes has moved to the right, α values as high as 55° yield mostly strikes. The effect continues in Figures 9c

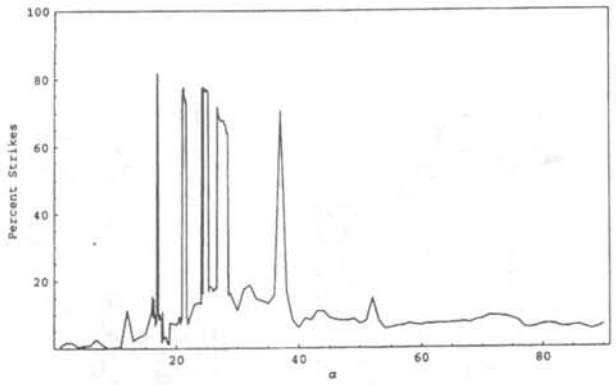

Figure 10
The percentage of time a strike occurs vs the initial position of the ball, α. For each value of α, the angle of the initial velocity, θ, ranges 180° in increments of 0.01°. Throughout, μ = 4.

and 9d. There is a gradual increase in the values of α that yield strikes as θ becomes more negative.

The nature of the strike zone

The data suggest that getting strikes is dependent on both the angle of the velocity of the ball and the initial collision point between the ball and the head pin. Figure 10 shows a combination of all the data. For each value of α, θ ranges 180° in increments of 0.1°. The total number of times the combination of a particular α and all increments of θ yielded a strike was calculated. Figure 10 presents the data as the percentage of times a strike occurs for each different initial contact point.

There are almost no values of α for which the percentage of time a strike occurs is zero. This means that it is possible to get a strike at virtually every value of α. However, the spikes that occur between α = 15° and α = 40° indicate that collision points for which the majority of the θ values would yield a strike. The values of α to which those peaks correspond are the points of collision toward which bowlers strive, those scattered thin spikes seen in Figure 10 make up the strike zone.

Figure 8 shows that there is no solid, thick range of a values for which the majority of θ values yield strikes, nor is there a single value of α for which 100% of the values of θ yields strikes. The opportunity exists to get strikes, but the position at which they are most likely to occur are thin ranges at which even 20-30% of the total values of the initial velocity angle do not yield strikes. The 'strike zone' that we have found is not a solid continuous range as the name might suggest, but a patch work of combined position and velocity values.

ACKNOWLEDGMENTS

The author would like to thank Professor Bill Titus for the opportunity to work on this project and for his support and guidance throughout. She also thanks Professors Rich Noer and Bruce Thomas for their helpful suggestions and encouragement.

REFERENCES

* Current address of author: 622 NW 52nd, Seattle, WA 98197, Christjb@carleton.edu
1. D. Hopkins, "Bowling", Encyclopedia of Sports Science, MacMillan Library Reference, (1997), p. 85-107.
2. Rules of the Game, the Diagram Group, St. Martin's Press, New York, (1990), p. 92-93.

FACULTY SPONSOR

Dr. Bill Titus
Department of Physics and Astronomy
Carleton College
One North College Street
Northfield, MN 55057-4025

DETECTOR EFFICIENCY FOR SMALL SOURCE-DETECTOR SEPARATIONS

Christopher Stapels *
Department of Physics
Alma College
Alma, MI 48801
received February 12, 1999

ABSTRACT

Quantitative neutron activation analysis requires accurate knowledge of the efficiency of the nuclear spectroscopy system. For maximum efficiency, the sample must as close to the detector as possible. We have developed an algorithm to calculate the efficiency of a γ-ray detector for small source-detector separations. The results compare favorably with data taken using ^{137}Cs and ^{22}Na sources.

INTRODUCTION

Neutron activation analysis is one of the more sensitive methods for determining the types and amounts of trace elements in a sample. The sample is made radioactive by irradiation in a neutron beam. Each different isotope in the activated sample emits γ-rays with characteristic energies. Measuring the number and energies of these γ-rays allows both quantitative and qualitative analysis.

Most neutron activation facilities make use of the large neutron flux available from a nuclear reactor. There are advantages, however, to using relatively low level neutron sources, not the least of which is not needing access to a nuclear reactor. To use a low level activation source, a highly efficient γ-ray spectroscopy system is required. To maximize the efficiency of the spectroscopy system, the sample must be placed as close to the detector face as possible. In these conditions, the geometry needed to determine detector efficiency becomes rather complicated.

DETECTOR EFFICIENCY

The efficiency of a detector is the ratio of the number of γ-rays detected to the number emitted by the source. The closer the source is to the detector, the greater the proportion of emitted γ-rays that hit the detector. When the separation, D, between the source and the detector is large compared to the radius of the detector face, the efficiency of the detector is the ratio of the area of the detector face to the area of a sphere whose radius is the source-detector separation:

$$eff \propto \frac{\pi R^2}{4\pi D^2} = \frac{R^2}{4D^2}, \qquad (1)$$

where R is the radius of the detector crystal as shown in Figure 1.

Three factors must be considered when the source is close to the detector:

° The area of the detector face is not a good approximation to the area of the spherical surface intersected by the detector face. In this case, the efficiency will no longer be

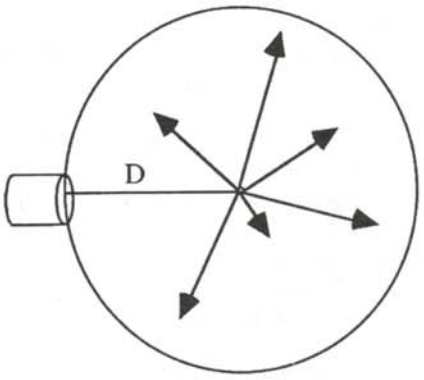

Figure 1
Geometry of a point source with a detector at a large distance D.

Christopher completed a B.Sc. in physics at Alma College with this research as his senior thesis. He is currently pursuing a Ph.D. in nuclear physics at Oregon State University. Current projects include experiments with similar equipment to measure neutron capture cross sections of radioactive elements and research involving an array of 20 similar germanium detectors at the Lawrence Berkeley National Laboratory in Berkeley, California.

proportional to $1/D^2$.

° The efficiency of the detector depends on the distance an incident γ-ray travels through the material of the detector crystal. The longer the path, the more likely it is that the γ-ray is detected. For large source detector separations, all incident γ-rays travel nearly parallel to the crystal axis. For sources close to the detector the distance traveled through the crystal depends on where the incident γ-ray hits the crystal face.

° The efficiency of the detector is a function of the energy of the incident γ-ray. The higher the energy, the more likely it will traverse a given distance in the crystal without being detected.

CALCULATIONS

The number of γ-rays that remain after passing through a distance, d, of a material is given by:

$$N_{left} = N_o e^{-\mu d}, \tag{2}$$

where N_o is the number of γ-rays incident and μ is the attenuation coefficient. This coefficient consists of three parts:

$$\mu = \sigma_{Compton} + \kappa_{pair\ production} + \tau_{photoelectric}. \tag{3}$$

In the photoelectric effect, the γ-ray imparts all of its energy to a free electron. This produces a current pulse in the detector which is proportional to the γ-ray ray energy. Compton scattering and pair production are competing mechanisms that produce unwanted detector noise.

The γ-rays that are detected are those that undergo the photoelectric effect. The number detected is:

$$N = N_o\left(1 - e^{-\tau(E)d}\right), \tag{4}$$

where $\tau(E)$ is a function of energy and d depends on where the γ-ray hits the face of the detector crystal. $\tau(E)$ is well known for materials such as lead, but values for germanium were not available to us. It can be found in terms of the coefficient for a known element, τ_1: [1]

$$\tau_2 = \tau_1 \frac{\rho_1}{\rho_2}\frac{A_1}{A_2}\left(\frac{Z_1}{Z_2}\right)^{n(E)}, \tag{5}$$

where Z_i is the atomic number, A_i the atomic weight and ρ_i the density. The exponent $n(E)$ is a function of energy and can be found in published graphs.[2] We used the exponential curve fitting routine from Cricket Graph to find $n(E)$.

The distance, d, in Equation 4, depends on where the incident γ–ray enters the detector crystal. We parameterize this dependence with the angle, θ, shown in Figure 2. Any γ–ray that exits the back face of the crystal passes through a volume we call the 'core'. An incident γ–ray not exiting the back face of the crystal would go through the 'edge'. The distance $d(\theta)$, for each region is given by

$$d(\theta)_{core} = \frac{L}{\cos(\theta)} \tag{6}$$

and

$$d(\theta)_{edge} = \frac{R - D\tan(\theta)}{\sin(\theta)}, \tag{7}$$

where L, R and D are shown in Figure 2. The limiting values of θ for the core and edge regions are functions of D:

$$\theta_{\max\ core} = \tan^{-1}\left(\frac{R}{L+D}\right) \tag{8}$$

$$\theta_{\max\ edge} = \tan^{-1}\left(\frac{R}{D}\right). \tag{9}$$

The number of γ–rays that are detected can be found by integrating over all possible paths through the crystal:

$$N_{core} = \int_0^{\theta_{\max\ core}} \left(1 - e^{-\tau(E)\,d_{core}(\theta)}\right) dN \tag{10}$$

$$N_{edge} = \int_{\theta_{\max\ core}}^{\theta_{\max\ edge}} \left(1 - e^{-\tau(E)\,d_{edge}(\theta)}\right) dN, \tag{11}$$

where

$$dN = \frac{1}{2} N_o \sin(\theta)\, d\theta, \tag{12}$$

is the number of γ–rays emitted between θ and θ + dθ. The integrals were evaluated usiing Simpson's rule in FORTRAN code. The total efficiency then becomes:

$$eff = \frac{N_{core} + N_{edge}}{N_o}. \tag{13}$$

COMPARISON WITH EXPERIMENTAL RESULTS

Our spectroscopy system consists of a high purity germanium (HPGe) detector coupled to a multichannel analyzer and a nuclide identifier software [3]. The heart of the system is a 3.486 cm diameter by 8.790 cm long HPGe crystal. The sample holder holds sources at nine different distances.

We compared the efficiency determined by our algorithm with data using a ^{137}Cs point source and a ^{22}Na point source placed various distances from the detector. At each

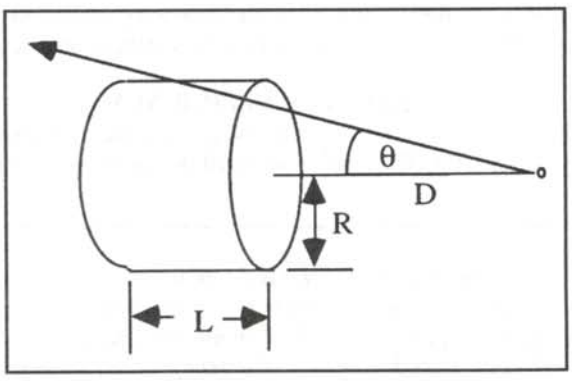

Figure 2
Geometry for a source close to a large crystal. The path length of an incident γ-ray through the detector depends on the crystal radius, R, the crystal length, L, the source-crystal separation, D, and the angle θ.

distance in the sample holder, we counted for 100 seconds of live time. This resulted in a statistically reliable number of counts in the smallest of the spectral peaks. The absolute activity of the sources was not known, so the predictions of the calculations were normalized to data at the largest distance from the detector, 10.4 cm.

The results, shown in Figure 3, demonstrate how well the algorithm reproduces the data. The largest error is for the 1274 keV γ-ray of ^{22}Na at a separation of 1.1 cm. Here the program overestimates the efficiency by 14%. We believe that the fault lies in our determination of the energy dependence of τ, the most uncertain element in the calculation. Still, the efficiencies are extremely sensitive to small changes at these separations. Uncertainty in the source-crystal separation may account for some of this relatively small error.

Figure 4(top) shows the improvement on the standard $1/D^2$ approximation. The data are normalized to 137Cs at 25 cm. At 10 cm, the $1/D^2$ calculation is in error by more than 50%; at one centimeter, the estimation is off by an order of magnitude. On the same scale, our predictions are virtually indistinguishable from the experimental data.

We activated a silver foil to determine the effect of an extended source on the efficiency of the detector. The foil had a radius of 2.5 cm, about a third of the radius of the

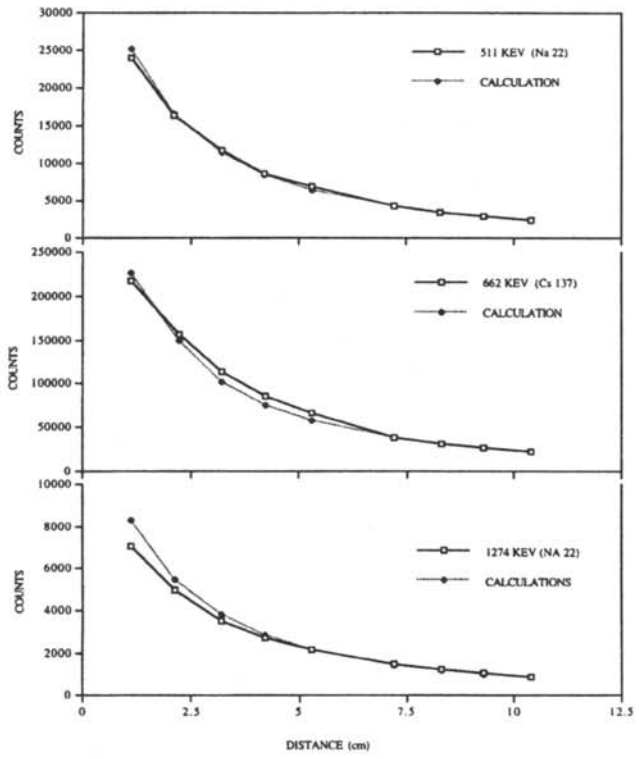

Figure 3
Comparisons of counts predicted from the efficiency code with data from ^{137}Cs and ^{22}Na sources.

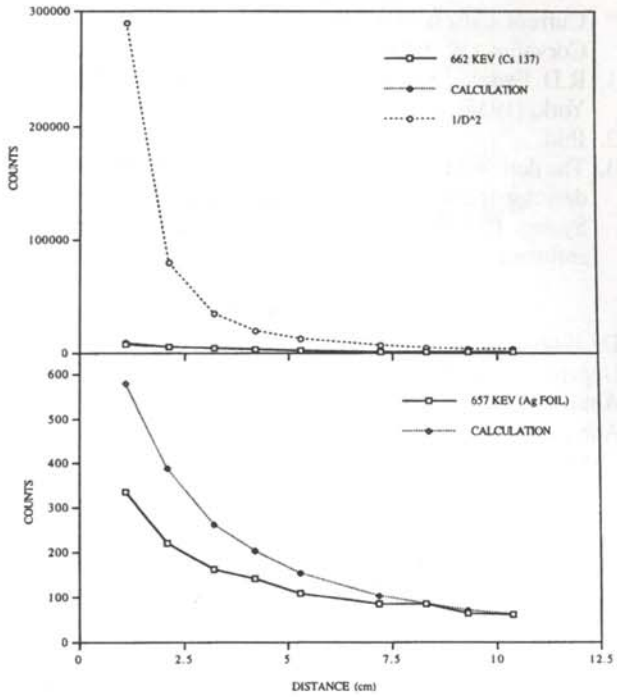

Figure 4
Top: Comparison of a $1/D^2$ calculation with experimental data and calculated estimates of the efficiency program. Bottom: Comparison of the data from an activated silver foil with the calculated estimates from the efficiency program.

detector crystal face. The results are shown in Figure 4. Note that the smaller number of counts leads to considerably more uncertainty in the data. The calculation overestimates the efficiency for this extended source. If a source on the axis has the most efficient counting geometry, then one would expect the efficiency for an extended source to become increasingly less than optimal as the separation decreases.

For quantitative activation analysis, the absolute efficiency of the detector is required. It is normal procedure for the efficiency of the detector to be specified relative to a standard NaI detector using the 1.33 MeV γ-ray of a ^{60}Co source placed 25 cm from the detector. The manufacturer's performance specifications for our detector give an efficiency rating of 73.2%. Our calculations give an efficiency of 68% of the standard NaI detector. This uncertainty is of the same order as the other uncertainties involved in a quantitative activation analysis and is acceptable.

ACKNOWLEDGMENTS

The author would like to thank Dr. Eugene Deci for making this project possible and Aaron Decker for useful insights about the geometric factors.

REFERENCES

* Current address of author: 2670 Garryanna Drive, #5, Corvallis, OR 97330 stapelsc@ucs.orst.edu

1. R.D. Evans, The Atomic Nucleus, McGraw-Hill, New York, (1955), p. 700.
2. Ibid.
3. The detector is an EG&G Ortec GEM Series HPGe detector. It was coupled with a Canberra Nuclear System 100 MCA. EG&G Ortec's Nuclide Navigator software was used to identify the peaks.

FACULTY SPONSOR

Dr. Eugene C. Deci
Department of Physics
Alma College
Alma, MI 48801
deci@alma.edu

SYNTHESIS AND ELECTRICAL CHARACTERIZATION OF CHEMICAL BATH DEPOSITED CdS ON ELECTRODEPOSITED $CuInSe_2$ JUNCTIONS

William Junek and Jason Underwood
Department of Physics and Space Sciences
Florida Institute of Technology
Melbourne, FL 32901
received March 27, 1999

ABSTRACT

$Cu_xIn_{2-x}Se_2$ (CIS) is one of the most promising absorber candidates for thin film solar cells due to its extremely high optical absorption coefficient and favorable photovoltaic properties. CdS is a well lattice matched window material for CIS. *P*-type CIS thin films were electrochemically deposited on Mo substrates and subsequently annealed in an Ar atmosphere. The *pn* junctions were formed using chemical bath deposition of CdS (which is naturally *n*-type) on the CIS. The electrical characteristics of the junction performance as a function of CdS solution pH were investigated.

INTRODUCTION

Thin film semiconductor technology has the capability of producing photovoltaic solar cells with efficiencies that are beginning to approach that of crystalline silicon cells. Thin film solar cells use minute amounts of semiconductor material deposited onto low cost, light weight substrates. Several cost-effective synthesis methods for producing these films have been developed.

Copper indium diselenide, $Cu_xIn_{2-x}Se_2$, (CIS) is a direct band gap semiconductor, with a band gap of approximately 1.1eV. [1] Due to native defects in its structure, it can be made *p* or *n* type by controlling the copper to indium ratio (*p*-type for Cu/In ratio greater than 1).[2] This material, with remarkably high absorption coefficient and appropriate band gap, is particularly well suited for use in a solar cell. [3] CIS currently holds the 'world record' for the highest thin film solar cell efficiency (17.7%) and has shown good environmental stability and radiation resistance. [4]

Cadmium sulfide (CdS) is a natural *n*-type material that is well lattice matched to CIS. [5] This material has a good transparency and band gap of approximately 2.4 eV. [6] These inherent material characteristics make it an ideal window layer for a CIS thin film photovoltaic solar cell. The wide band gap of CdS ensures that the majority of the incident visible light will pass through the CdS layer where then it can be absorbed by the CIS. Because of the high absorption coefficient of CIS, the photons will be absorbed soon after entering the CIS and, therefore, near the *pn* junction's depletion region. The carriers that are created in the depletion region, or diffuse to that region, will be swept out due to the built-in voltage of the junction and produce the desired photocurrent.

Electrochemical deposition (ECD) and chemical bath deposition (CBD) are both simple and low cost fabrication techniques that can be used to produce photovoltaic devices. Conventional methods of semiconductor device fabrication, such as molecular beam epitaxy or chemical vapor deposition, are considerably more complicated and expensive to implement than these techniques. ECD has been used to deposit *p*-type CIS films on molybdenum substrates. [7] The deposition potential can be used to control the Cu to In ratio in the films, and thus their

William Junek is an Electrical Engineering major at the Florida Institute of Technology where he is expected to graduate in the fall of 1999. He currently is working as a summer research assistant at the NASA Glenn Research Center at Lewis Field. Future plans include employment at Raytheon Systems Company and graduate studies in electrical engineering or material physics.

Jason Underwood is an Electrical Engineering major at the Florida Institute of Technology where he is expected to graduate in the spring of 2000. He is currently working as a summer research assistant at the National Renewal Energy Laboratory. Future plans include graduate studies either in physics or semiconductor materials science.

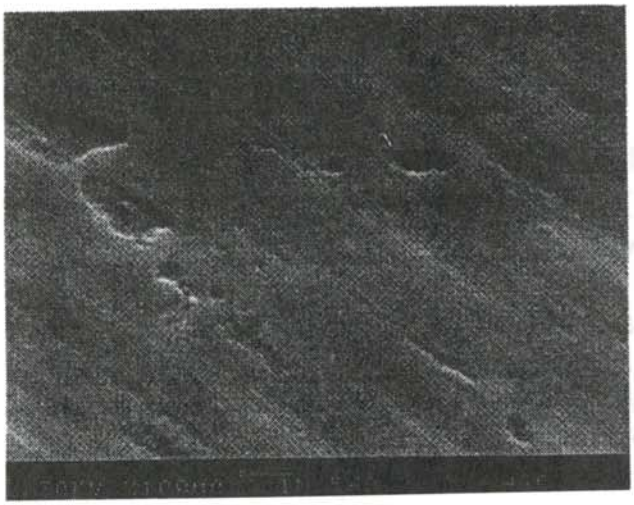

Figure 1
SEM micrograph of the Mo substrate.

majority carrier type and density. CBD has been developed to epitaxially grow a naturally *n*-type CdS layer on an already existing *p*-type CIS layer to form a *pn* junction between the two materials. [8] This procedure only requires the placement of the sample in the CdS solution for the deposition to take place. However, the quality of the resulting CdS films vary significantly with the pH, temperature and composition of the bath used. [9]

EXPERIMENT

Several substrates were cut from molybdenum stock, cleaned and labeled. Molybdenum was chosen as the substrate material since it makes good Ohmic contact to CIS and does not react with the deposition solution. A CIS solution, consisting of 500 ml deionized water, 0.0746 g (1mM) Cu, 2.5845 g (10 mM) In, 0.279 g (5mM) SeO_2, 3.676 g (25 mM) sodium citrate and 10% (per total volume) denatured alcohol, was prepared. The substrate was placed in a holder mounted on a rotary motor set to run at 500 rpm. The sample holder was submerged in the CIS solution and all bubbles remaining on the exposed surface of the substrate were removed to ensure a uniform deposition. A potentiostat set to -1.2 V with respect to a saturated calomel electrode (SCE) was used to grow the *p*-type CIS films. This potential produces a slightly Cu rich film (*p*-type film). Using Faraday's law, a deposition time of 600 seconds should yield a CIS film approximately 1 micron thick. [1]

To reduce the number of inherent defects that occur in the electrochemical deposition process, one set of samples was annealed at a temperature of 400C for one hour and a second set at 600C. The annealing process was performed in a flowing atmosphere of argon to eliminate the possibility of the sample oxidizing under the extreme temperature. After the annealing process, the samples were masked with red glyptol enamel to ensure that the top surface of the molybdenum substrate (the portion not coated with CIS) was electrically insulated from the CdS layer which would be deposited next.

Two solutions were prepared for the CdS chemical bath deposition: 50 ml of deionized water and 5.33 g (0.2 M) $Cd(CH_3C00)_2$ (cadmium acetate); 50 ml of deionized water and 3.86 g (0.5M) $SC(NH_2)_2$ (thiourea). The solutions were heated separately and then mixed together. Ammonium hydroxide was then added to the mixed solutions to raise the pH to the desired value and initiate the deposition. The solution temperature was maintained at 80 C for all but one sample, which was held at 90 C.

A series of *pn* junctions were made on the *p*-type CIS films by depositing the CdS at pH values of 8, 9 and 10. Each CBD was performed for 5 minutes. The thickness of the CdS layer should be on the order of 10^{-8} m thick. [7] Following the deposition, the samples were removed from the solution and rinsed under deionized water. The sides of each sample were sanded to eliminate the possibility of a short between the CdS layer on the top and the Mo

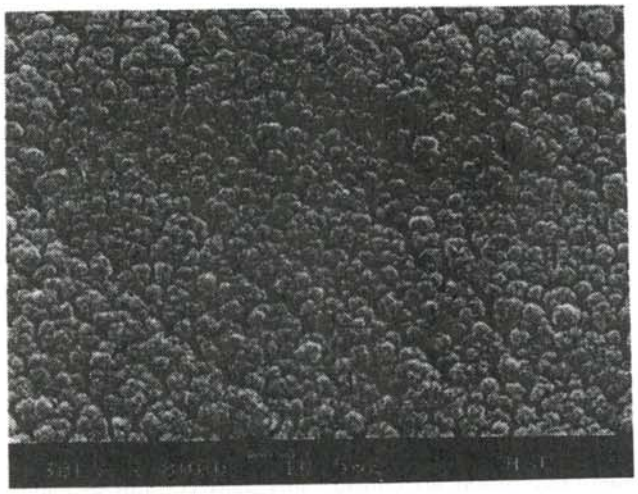

Figure 2
SEM micrograph of a CIS thin film that was electrodeposited at -1.2 V vs SCE and annealed in Ar at 600C for 1 hour.

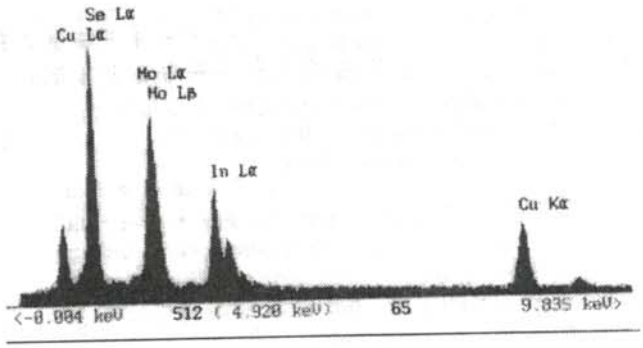

Figure 3
EDS spectrum for CIS electrodeposited at -1.2 V vs. SCE on Mo and annealed at 600C in flowing Ar.

substrate.

The surface morphology of the CIS and CdS films was examined using a scanning electron microscope (SEM). Energy dispersive spectroscopy (EDS) was performed to determine the elemental composition of the films. Unfortunately, due to the overlapping spectroscopic lines of Cd with In and S with Mo, a precise stoichiometric determination of the CdS film was not possible. The overlapping signals seen in EDS is less of a problem in Auger spectroscopy because the Auger electrons are only due to the surface of the material. We performed Auger electron spectroscopy on the CdS on CIS films. A depth profile of the stoichiometry is possible by repetitively determining the surface stoichiometry and etching the surface using argon ion bombardment.

To perform the current vs voltage (I-V) characterizations of the *pn* junctions, metal contacts (either GaIn eutectic or silver paint) were applied to the CdS layer of each sample. The molybdenum substrate served as the other metal contact to complete the circuit.

RESULTS

Figure 1 shows the SEM of the substrate. The surface is generally smooth with shallow pits on the order of 1 square micron in area. The polishing striations running diagonally across the micrograph are apparent.

Figure 2 shows the SEM micrographs of the CIS films They show a dense polycrystalline film with an average grains size of less than 1 micron. The growth of the grains appears to be influenced by the polishing marks. Several long grain boundaries which are parallel to the polishing marks can be seen.

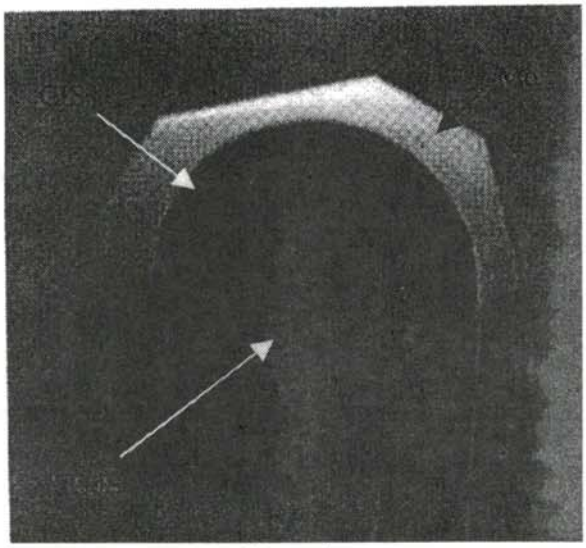

Figure 4
Photograph of the CdS on CIS sample The CIS is the circular dark area and the CdS is the lighter circle.

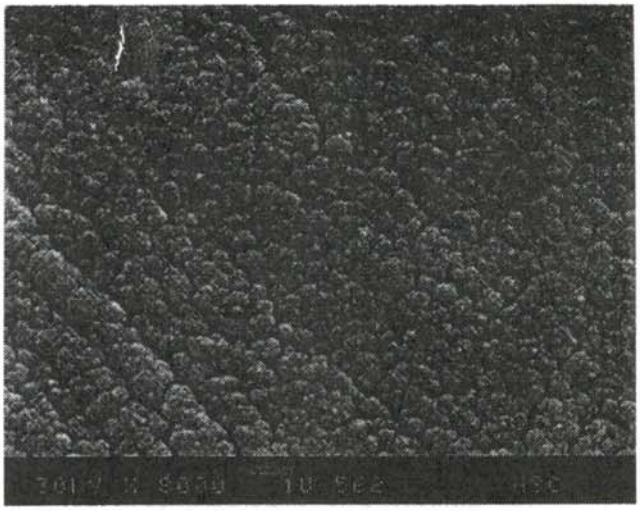

Figure 5
SEM micrograph of chemical bath deposited CdS on electrodeposited CIS.

The x-ray spectrum from the EDS performed on the CIS film shown in Figure 2 is presented in Figure 3. The electron beam energy was set to 30 keV and a tilt angle of 50° was used to collect the spectrum. Standardless ZAF analysis of the spectrum yielded the following atomic percentages: [Cu] = 24.90; [In] = 21.27; [Se] = 53.83. This is in reasonably good agreement with the 1:1:2 proportion expected for stoichiometric CIS. The film has a Cu to In ratio that is greater than 1, which corresponds to a *p*-type film.

Figure 4 is a photograph of a typical CdS on CIS on Mo sample. The Mo substrate is an octagonal shape. The outer edge of the black CIS film is circular. The film is extremely black, attesting to its optical absorptive properties. The lighter colored circular deposit of CdS is seen at the center of the CIS.

Figure 5 shows a SEM micrograph of the CdS film deposited at a pH of 8 and temperature of 90C onto an electrodeposited CIS film. The film is somewhat smoother than the underlying CIS, but appears to follow the underly-

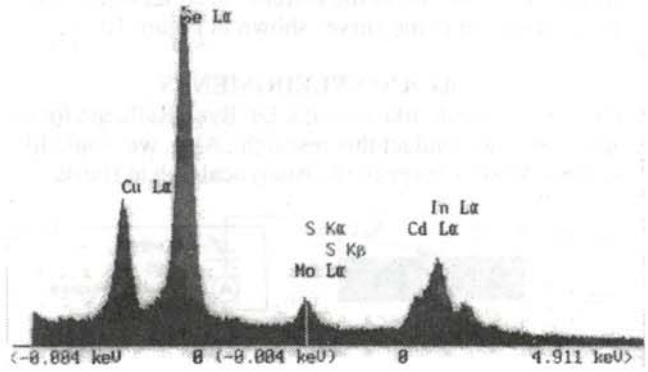

Figure 6
EDS spectrum of chemical bath deposited CdS on CIS.

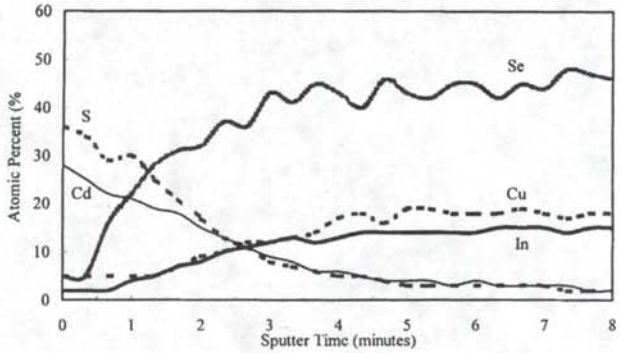

Figure 7
Auger depth profile of CdS on CIS pn junction.

ing CIS grain structure. We were able to identify the Cd and S peaks in an EDS done on the CdS over layer by reducing the electron beam energy to 10 keV and using an extreme tilt angle of 80°. Figure 6 shows the region of the spectrum where the Cd peak is observable.

Figure 7 shows the results of the Auger spectroscopy. The surface has relatively equal amounts of Cd and S, although it was slightly S rich. A smooth transition from CdS on the surface to CIS underneath was observed as we sputtered away the surface and descended through the film.

A schematic of the experimental setup for the I-V measurements is shown in Figure 8. A distinction was noticed between the two contact materials used. The silver paint contacts provided a smaller turn-on and reverse-bias breakdown voltages than the GaIn eutectic contacts (see Figure 9). It is possible that the solvent in the silver paint reacted with the films and penetrated the grain boundaries, leading to a shorting of the junction and a decrease in junction performance.

The results of the I-V characterizations are shown in Figure 10. All the junctions measured had a similar reverse-bias response. However, the pH of the CdS solution had a significant effect on the forward-bias behavior. This suggests that the number of defects in the CdS or at the CdS/CIS interface increases with the solution pH and is manifested in the increase in series resistance that is observed in the curves shown in Figure 10.

ACKNOWLEDGMENTS

The authors would like to thank Dr. Ryne Raffaelle for the opportunity to conduct this research. Also, we would like to thank Mike Schlepr of the Analytical Lab at Harris Semiconductor for access to their characterization facilities. Finally, we would like to acknowledge the Department of Physics and Space Sciences at Florida Institute of Technology for their support in this work.

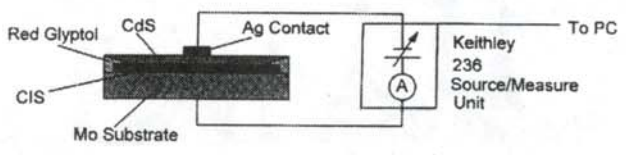

Figure 8
Schematic diagram of the apparatus used for to take the V-I measurements.

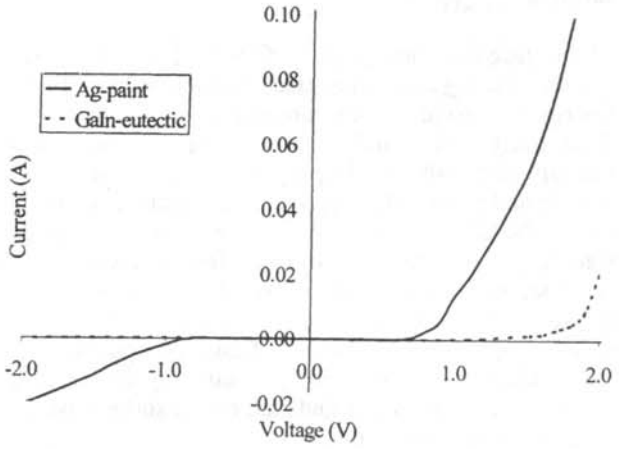

Figure 9
I-V curves for CdS on Cis pn junctions using silver paint and GaIn contacts.

REFERENCES

1. R.P. Raffaelle, J.G. Mantovani, S.G. Bailey, A.F. Hepp, E.M. Gordon and R. Haraway, Materials Research Society Proceedings, 495, (1997), p. 383.
2. A. Rocket and R.W. Birkmire, J. Appl. Phys., 70 (1991) p. R81.
3. R Marudachalam, R.W. Birkmire and H. Hichri, J. Appl. Phys., 82, (1997), p. 2896.
4. K. Zweibel, H. Ullal and B. von Roedern, 25` IEEE Photovoltaics Specialists Conference (IEEE, New York), 1996.

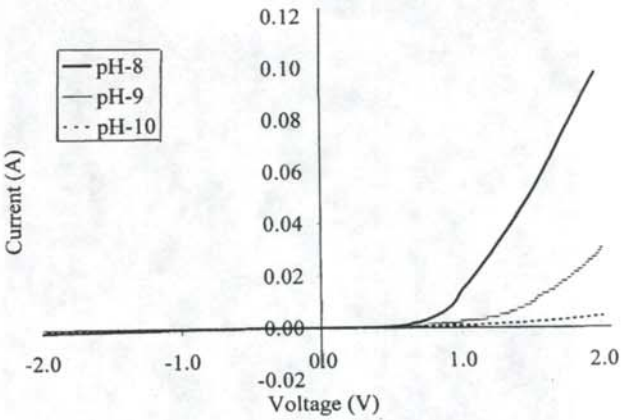

Figure 10
I-V curves for CdS on CIS ph junctions as a function of the CdS solution pH. The shallower forward biased curve implies a higher series resistance.

5. M. L. Breen, J.T. Woodward IV, D.K. Schwartz and A.W. Apblett, Chem. Mater., 10 , 3 (1998), p. 710.
6. T. Walter, M. Ruckh. K.O. Velthaus and H.W. Schock, 11th Photovoltaics Solar Energy Conference, (1992), p. 124.
7. R.P. Raffaelle, J.G. Mantovani, R. Friedfeld, S.G. Bailey and S.M. Hubbard, 26th IEEE Photovoltaics Specialists Conference, (IEEE, New York) 1997.
8. O. Savadogo, Sol. Energy Mat. and Sol. Cells, 52, (1998), p. 361.
9. S. Kuranouchi, T. Nakazawa, A. Ashida and N. Yamamoto, Sol. Energy Mat. and Sol. Cells, 35, (1994), p. 185.

FACULTY SPONSOR

Dr. Ryne P. Raffaelle
Department of Physics and Space Sciences
Florida Institute of Technology
Melbourne, Fl 32901
rpr@pss.fit.edu

Due to an error while producing Volume 17 #1, part of the paper:

SHOE-STRING INTERFEROMETRY

by Jenny Flood, Ryan Scheetz and Marta Sieradzan of the Department of Physics at Central Michigan University

was not printed. The editor apologizes for this error. In the right column is the complete page 24 of this paper.

= 3.08 gm/m, ϖ = 43.72 Hz, and mass m of each of the 'reflectors' = 7 gm.

Substituting these values into Equation 14, we get a transmission coefficient of $T = 0.016$. Assuming no loss, the reflection coefficient $R = 0.994$. Using 'eye ball' measurements, we estimated the amplitude ratio between the intracavity wave and the incident wave to be between 10 and 20. This gives an intracavity intensity increase between 100 and 400. From the graph shown in Figure 3, we found that to obtain such an intracavity intensity increase, one needs a reflectivity coefficient of approximately 0.995, consistent with our calculated reflection coefficient.

This is a simple and effective demonstration of the energy trapping characteristic of the Fabry-Perot cavity. The point masses act as partially reflecting mirrors. The string interferometer displays the intracavity intensity increase at resonance. The simple wave model of this system models the experiment well.

ACKNOWLEDGMENTS

The authors would like to thank to Central Michigan University for financial support for this work. Jenny Flood was sponsored with the CMU Office of Research Summer Scholar program and Ryan Scheetz with the faculty advisor's research grant.

REFERENCES

* Current address of author: R. Scheetz: Physics Department, Central Michigan University, Mt. Pleasant, MI.
§ Current address of author: M. Sieradzan: School of Engineering, University of Michigan, Ann Arbor, MI
† Current address of author: J. Flood: 1500 Rose St. Apt#2, Bay City, MI 48708.

1. See, for example, F. Pedrotti and L. Pedrotti, Introduction to Optics, 2nd Ed., (Prentice-Hall), 1993, pp,. 233-239.
2. C.S. Wood, et al., "Measurement of Parity Nonconservation and an Anapole Moment in Cesium", Science, 275, (March 21, 1997), pp. 1759-1763.
3. S. Pamley, et al., "Vibrational Properties of a Loaded String", Am J. Phys., 63, (June 1995), pp. 547-553.
4. P. Allen and J. Kelner, "Evolution of a Vibrational Wave Packet on a Disordered Chain", Am. J. Phys., 66, (June 1998), pp. 497 - 506.
5. See, for example, J. Taylor and C. Zafiratos, Modern Physics for Scientists and Engineers, (Prentice-Hall), 1991, pp. 200-202.

FACULTY SPONSOR

Dr. Andrzej Sieradzan
Department of Physics
Central Michigan University
Mt. Pleasant, MI 48858

PREPARING A MANUSCRIPT FOR PUBLICATION

Rexford E. Adelberger, Editor

Perhaps the most important thing for you to keep in mind when you write a manuscript which you intend to submit for publication to the Journal of Undergraduate Research in Physics is that the audience that will be reading the paper is junior or senior physics majors. They are knowledgeable about physics, but unlike you, they have not spent as much time trying to understand the specific work which is being reported in your paper. They also can read English well, and expect the paper to be written by a colleague, not a robot or an 'all-knowing' computer. There is a big difference between the comments you write in the margin of your lab notebook or what you might write in a technical brief and what you should present in a paper for publication in a scientific journal.

There is a significant difference between a Journal article and keeping a journal. Your laboratory data book should be the journal of what you did. It contains all the data, what you did (even if it was an attempt that turned out to be wrong), as well as comments as to what you were thinking at that time. The Journal article is an discussion of how you would do the research without excursions along blind alleys and hours spent collecting data that were not consistent. The reader does not have to be able to completely reproduce the work from the Journal article. The reader should be able to understand the physics and techniques of what was done.

How a person uses Journal articles to find out about new ideas in physics is often done in the following way. A computerized search, using key words in abstracts, is performed to find what work others have done in the area of interest. If the abstract seems to be about the question of interest, the body of the paper is tracked down and read. If the reader then wants to find out the finer details of how to reproduce the experiment or the derivation of some equation, the author of the paper is contacted for a personal in-depth conversation about the more subtle details.

The general style of writing that should be followed when preparing a manuscript for publication in the Journal is different from what you would submit to your English literature professor as a critique of some other work. The narrative of the paper is intended to do three things: 1) present the background necessary for the reader to appreciate and understand the physics being reported in the paper; 2) discuss the details of what you did and the implications of your work; 3) lead the reader through the work in such a way that they must come to the same concluding points that you did. When finished with your paper, the reader should not have to go back and try to decide for themselves what you did. Your narrative should lead them through your work in an unambiguous manner, telling them what to see and understand in what you did. The interpretation of the data or calculations should be done by the writer, not the reader. The interpretation of your results is the most important part of the paper.

You should take care to make sure that the material is presented in a concise logical way. You should make sure that your sentences do not have too many dependent clauses. Overly complicated sentences make the logic of an argument difficult to follow. You should choose a paragraph structure that focuses the attention of the reader on the development of the ideas.

A format which often achieves these aims is suggested below:

ABSTRACT : An abstract is a self contained paragraph that concisely explains what you did and presents any interesting results you found. The abstract is often published separately from the body of the paper, so you cannot assume that the reader of the abstract also has a copy of the rest of the paper. You cannot refer to figures or data that are presented in the body of the paper. Abstracts are used in computerized literature searches, so all key words that describe the paper should be included in the abstract.

INTRODUCTION: This is the section that sets the background for the important part of the paper. It is not just an abbreviated review of what you are going to discuss in detail later. This section of the narrative should present the necessary theoretical and experimental background such that a knowledgeable colleague, who might not be expert in the field, will be able to understand the data presentation and discussion. If you are going to use a particular theoretical model to extract some formation from your data, this model should be discussed in the introduction.

Where appropriate, factual information should be referenced using end-notes. When presenting background information, you can guide the reader to a detailed description of a particular item with the statement such as: *"A more detailed discussion of laminar flow can be found elsewhere [1]"*. If you know where there is a good discussion of some item, you don't have to repeat it, just guide the reader to the piece.

How one proceeds from this point depends upon whether the paper is about a theoretical study or is a report on an experiment. I will first suggest a format for papers about experimental investigations and then one that describes a theoretical derivation.

Experimental Investigations

THE EXPERIMENT: This section guides the reader through the techniques and apparatus used to generate the data. Schematic diagrams of equipment and circuits are often easier to understand than prose descriptions. A statement such as *"A diagram of the circuit used to measure the stopping potential is shown in Figure 6"* is better than a long elegant set of words. It is not necessary to describe in words what is shown in a diagram unless you feel that there is a very special part which should be pointed out to the reader. If special experimental techniques were developed as part of this work, they should be discussed here. You should separate the discussion of the equipment used to measure something from your results. This section should not include data presentations or discussions of error analysis.

DATA PRESENTATION AND INTERPRETATION OF RESULTS: This is the most important section of the paper. The data are the truths of your work. This section should lead the reader through the data and how errors were measured or assigned. The numerical data values are presented in tables and figures, each with its own number and caption, e.g.. *"The results of the conductivity measurements are shown in Table 3"*. It is difficult to follow narratives where the numerical results are included as part of the narrative. Raw, unanalyzed data should not be presented in the paper. All figures and tables should be referred to by their number. Any figure or table that is not discussed in the narrative should be eliminated. Items which are not discussed have no place in a paper.

A Theoretical Study

THE MODEL: This part should consist of a theoretical development of the constructs used to model the physical system

under investigation. Formulae should be on separate lines and numbered consecutively. The letters or symbols used in the equations should be identified in the narrative, e.g.. *The potential can be approximated as:*

$$W \approx Z - \sigma(\rho) \ , \qquad (1)$$

where Z is the number of protons and σ is the screening constant that is dependent on the charge density, ρ, of the inner electrons of the K and L shells. If you wish to use this formula at a later time in the narrative, you refer to it by its number, e.g.. *"The straight line fit shown in Figure 3 means that we can use Equation 1 to extract a value of..."*

CALCULATIONS: This section presents a summary and discussion of the numerical results calculated from the model. The results should be presented in tables or graphs, each with a caption. A table or graph that is not discussed in the narrative should be eliminated. Data that are not interpreted by the writer have no place in a paper. One should reference numerical results that are used in the calculations and come from previous work done by others .

The following sections pertain to both types of papers.

CONCLUSIONS: It is indeed rare that one can come to clear and meaningful conclusions in one paper. I do not know of many papers where this section should be included.

REFERENCES: All references, numbered in order from beginning to end of the paper, are collected together at the end of the paper. You should be aware of the following format:

If the reference is a text-

1. A.J. Smith and Q.C.S. Smythe, Electromagnetic Theory, Addison Wesley, New York, (1962), p. 168.

If the reference is a journal-

2. J. Boswain, Journal of Results, 92, (1968), pp. 122-127.

If the reference is unpublished-

3) R.J. Ralson, private communication.

ACKNOWLEDGMENTS: This short section should acknowledge the help received (that is not referenced in the previous section) from others. This is where you would give credit to a lab partner or someone in the machine shop who helped you build a piece of equipment.

OTHER ADVICE

TABLES AND FIGURES are placed by the layout editors at the corners of the page to make the format attractive and easy to read. Often a figure is not on the same page as the discussion of the figure. Each table or figure should be numbered and have a caption which explains the figure. Readers scan papers by looking at the figures and data tables before they read the narrative of the work. Take care to put enough information in the caption of a figure or table so that the reader can get some feeling for the meaning of the data presentation. All lines shown on graphs should be identified, e.g.. *"The dashed line is drawn to guide the eye"* or *"The solid line is a fit to the data using the Ising model"*

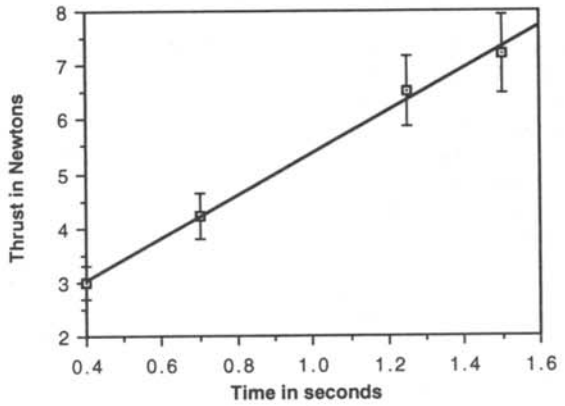

Figure 1

A graph of the measured thrust of a D-2 model rocket engine as a function of time. The line drawn is the least squares fit straight line to the data.

State	*Experimental eV*	*Theoretical eV*
3S	*5.15±01*	*5.13*
4S	*1.89±02*	*1.93*
3P	*2.96±02*	*3.02*

Table 1

Energy states found in the numerical search. The accepted values for these states are also listed.

An example of a graph of a set of data is shown in Figure 1. The graph is sized by the range of data points. The bottom left point does not have to be the point (0,0). Error bars are shown with the data points. A graph with all the data points clustered in one small corner and lots of white space does not help the reader get a feeling of the dependence of your data. Be careful that the figures you present are not too busy; too much information on a figure makes it difficult to pick out the important parts.

NUMBERS AND UNITS Any experimentally measured data presented in tables (such as shown in Table 1), should include an uncertainty. You should use scientific notation when presenting numbers, $(7.34 \pm .03)\text{x}10^7$ eV. Take care that you have the correct number of significant digits in your results; just because the computer prints out 6 digits does not mean that they are significant. You should use the MKS system of units.

STYLE It is often helpful to make a flow chart of your paper before you write it. In this way, you can be sure that the logical development of your presentation does not resemble two octopuses fighting, but that it is linear.

One generally writes the report in the past tense. You already did the experiment. You also should use the third person neuter case. Even though you might have done the work by yourself, you use "we". e.g.. *"We calculated the transition probability for..."* It is often confusing when you begin sentences with conjunctions. Make sure that each sentence is a clear positive statement rather than an apology.

There are a few words or phrases you should be careful of using. ***Fact*** - this is a legal word. I am not sure what it means in physics. ***Proof or prove*** - These words are meaningful in mathematics, but you can't prove something in physics, especially experimental physics. ***The purpose of this experiment is...*** Often it is necessary to do the experiment to complete the requirements for your degree. You do not need to discuss the purposes of the experiment. ***One can easily show that...*** - Don't try to intimidate the reader. What if the reader finds it difficult to show? Remember that the reader of your paper is a senior in college! ***It is obvious that... or One clearly can see....*** - Such statements only intimidate the reader that does not find your work trivial. What is obvious to someone who has spent a lot of time thinking about it may not be obvious to the reader of your paper. ***Data*** is the plural form of the noun datum. *"The data are ..."* or *"The data show that ...."*

The Journal of Undergraduate Research in Physics

The Journal of Undergraduate Research in Physics is the journal of Sigma Pi Sigma and the Society of Physics Students. It is produced by the Physics Department of Guilford College, Greensboro NC 27410. Inquiries about the journal should be sent to the editorial office.

The Journal of Undergraduate Research in Physics ISSN 0731-3764

Editorial Office -
The Journal of Undergraduate Research in Physics
Physics Department
Guilford College
Greensboro, NC 27410
336-316-2279 (voice)
336-316-2951 (FAX)

Editor -
Dr. Rexford E. Adelberger
Professor of Physics
Physics Department, Guilford College
Greensboro, NC 27410
Rex@Guilford..Edu

Managing Editor -
Mr. Ari M. Betof
ABetof@Guilford.Edu

The Society of Physics Students

National Office -
Dr. Philip Hammer, Director
Ms. Sonja Lopez, SPS Supervisor
Society of Physics Students
American Institute of Physics
1 Physics Ellipse
College Park, MD 20740
301-209-3007

President of the Society -
Dr. Gary White
Department of Physics
Northwestern State University

President of Sigma Pi Sigma -
Dr. Thomas Olsen
Department of Physics
Louise & Clark College